

Simulation of Viscoelastic Fluids: Couette–Taylor Flow

Raz Kupferman

*Mathematics Department, Lawrence Berkeley National Laboratory, 1 Cyclotron Road,
50A-2152, Berkeley, California 94720
E-mail: raz@math.lbl.gov*

Received May 23, 1997; revised January 22, 1998

We present a numerical scheme for viscoelastic flow based on a second-order central differencing method recently introduced in the context of incompressible newtonian flow; the incompressibility constraint is treated with the projection method. The result is a simple and efficient scheme that is readily adaptable to a wide class of differential constitutive equations and flow geometries. We implement the new method on Couette–Taylor flow for a fluid governed by the Oldroyd-B constitutive equations. We simulate transient flow in a domain that includes at least eight wavelengths during many hundreds of natural periods. For weak elasticity, a stationary instability leading to Taylor vortices is observed. For a regime of parameters where both inertia and elasticity are important, the instability is oscillatory. In both cases the early stage growth rates are compared to linear stability calculations, showing good agreement. The oscillatory instability is fourfold degenerate and gives rise to two bifurcating branches: an axially traveling wave and a standing wave; only one of these solutions is stable. In the early stages of the instability, there is generally a combination of traveling and standing waves, depending on the initial conditions. As nonlinearities become important, the flow spontaneously breaks into coexisting regions of upward- and downward-going waves. Such flow can persist for long times, until the globally stable traveling wave takes over and a limit cycle is reached. © 1998 Academic Press

Key Words: viscoelastic flow; Couette–Taylor; finite differences; Hopf bifurcation.

CONTENTS

1. *Introduction.*
2. *The Equations of Motion.*
3. *The Couette–Taylor problem.*
4. *The numerical scheme.* 4.1. The projection method. 4.2. Interior cells. 4.2.1. Piecewise-linear reconstruction. 4.2.2. Calculation of $\psi_{i+1/2,j+1/2}^{n+1}$. 4.2.3. Hodge projection. 4.3. Boundary cells. 4.3.1. Grid structure. 4.3.2. Piecewise-linear reconstruction. 4.3.3. Calculation of $\psi_{i+1/2,j+1/2}^{n+1}$. 4.3.4. Hodge projection. 4.4. Time step selection.

5. *Stability.* 5.1. Linear stability analysis: background. 5.2. Beyond linear stability. 5.3. Linear stability: A finite differences eigenvalue solver. 5.4. Results.
6. *Numerical results.* 6.1. The stationary transition. 6.2. The oscillatory transition.
7. *Discussion.*

1. INTRODUCTION

Despite much progress in the prediction of fluid flow, viscoelastic flow is an example of a field in which the numerical techniques are still generally inadequate to describe flows in regimes of technological importance; this inadequacy is particularly acute when one considers flows with large stress gradients and for time-dependent flows. The goal of this paper is to exhibit a numerical method applicable to time-dependent viscoelastic flow under a wide range of flow conditions.

Viscoelastic fluids are polymeric materials in which the state-of-stress depends on the history of the deformation, in contrast to newtonian fluids in which the stress depends only on the instantaneous rate of deformation. Viscoelastic fluids may exhibit behavior that differs significantly from that of newtonian fluids; some of the peculiar flow phenomena are the well-known “rod-climbing,” extrudate swell, and “tubeless siphon.”

In many cases, the understanding of viscoelastic rheology is poor. One reason is the approximate nature of the constitutive equations [1]; there is no systematic way of determining the range of validity of a model in describing a specific fluid. All models are at most reasonable approximations in a limited range of flow conditions. Even if the validity of the constitutive equation is taken for granted, its mathematical complexity rarely allows the derivation of analytical results, except for the simple cases of viscometric flows and for small perturbations about such flows. It is in this context that direct numerical simulations are called for, both to test constitutive models and as a tool to analyze and predict rheological phenomena.

Polymeric liquids are also known to exhibit flow instabilities that are not observed in low molecular weight liquids (for reviews see [2, 3]). Such instabilities are often the limiting factor in fabrication processes, and their understanding is therefore of practical importance. In this paper we study a particular system that exhibits interesting instabilities: Couette–Taylor flow of a viscoelastic fluid confined between two concentric rotating cylinders.

The rich sequence of instabilities of the Couette–Taylor flow in newtonian fluids is well understood [4, 5]. The viscoelastic Couette–Taylor instability has also received much attention for the last three decades; the main results are summarized in Section 5. In brief, three basic flow regimes have been identified: an inertial regime, a purely elastic, or inertia-less regime, and an intermediate inertio-elastic regime. In the first case, the primary instability is stationary; the primary azimuthal flow is taken over by a steady-state structure of Taylor vortices. In the two remaining cases the instability is oscillatory, or overstable; the new flow pattern emerges through a Hopf bifurcation.

All the above instabilities can be predicted by linear stability analysis [6–14]. Moreover, bifurcation theory can predict part of the bifurcation structure on the basis of general considerations, for example on the analysis of the symmetries of the equations of motion [15, 14]. Thus, one can show that the Hopf bifurcation is fourfold degenerate, and as a result two branches of solution can emerge: axially traveling waves or standing waves. If both branches are supercritical (as evidence shows), one and only one of them is stable. Which

of the bifurcating branches is stable cannot be resolved by bifurcation theory. It is partly to clarify this issue that numerical studies of time-dependent Couette–Taylor flow have been pursued [16, 17].

Northey *et al.* [16] used a finite-element method to solve the upper-convected Maxwell equation in the purely-elastic regime; i.e., the inertial terms were discarded. Beyond the bifurcation point, the flow was found to attain an oscillatory limit cycle; a plot of the amplitude of the limit cycle versus the bifurcation parameter confirmed that this bifurcation is supercritical. We note the limitations of these calculations: (i) the simulations were performed in a domain which contains only one wavelength. In other words, the wavelength was constrained by the geometry rather than selected dynamically. (ii) The initial condition consisted of the primary azimuthal flow, on top of which was superimposed the “most dangerous mode,” as predicted by linear stability analysis. To speed up the simulations, the amplitude of this initial instability was taken to be large and then allowed to relax down. This again may force a certain solution to be selected and may not allow the “naturally selected” solution to develop spontaneously. (iii) Limiting the size of the domain to a single wavelength has as consequence that the wavenumber separation between neighboring Fourier modes is large. Hence one needs to exceed significantly the instability threshold to observe mode interactions; such interactions are likely to occur in any realistic system because the stability spectrum is typically very flat. Note that even though these simulations were performed on meshes of the order of 20 points, the conclusion was that “*calculations with substantially finer discretizations are prohibitively expensive.*”

Avgousti *et al.* [17] used a pseudospectral method to simulate time-dependent flows both in the purely elastic and in the inertio-elastic regimes. As in [16], the computational domain was a single wavelength; the most refined discretization was of 16 axial points and 33 radial points. Their findings are that in the purely elastic regime it is the standing wave solution which is selected, whereas the traveling wave solution is selected in the intermediate inertio-elastic regime. When the initial condition was taken to be the unstable oscillatory mode (e.g., a standing wave state in the inertio-elastic regime), the oscillations were found to grow exponentially, causing the calculation to eventually breakdown; all attempts failed to produce a stable limit cycle solution. Although these calculation were performed on a supercomputer, the ultimate conclusion was that “*the increased computational workload resulting from a small time step size and an anticipated long transient make these calculations impractical with the available computational resources.*”

The above examples demonstrate well how indispensable it is to develop computational methods capable of simulating such flows under realistic conditions.

In recent years, Tadmor and co-workers introduced a sequence of new schemes, which can be viewed as higher order sequels of the Lax–Friedrichs (LxF) scheme. The new method retains the relatively simple form of central-difference schemes, but does not suffer from the poor resolution of the first-order LxF scheme. Nessyahu and Tadmor originally constructed a second-order scheme for systems of conservation laws in one spatial dimension [18]. This work was then extended to higher orders [19] and to several spatial dimensions [20].

The two-dimensional Euler equations in their vorticity formulation were treated along these lines by Levy and Tadmor, both in second- and third-order versions [21, 22]. A method based on the more practical velocity formulation was developed by Kupferman and Tadmor (KT) [23]; the pressure was calculated with the projection method [24, 25]. This new scheme

was tested on the classical doubly-periodic shear layer and on longitudinal flow in a channel. Its performance was compared to that of upwind schemes and was found to give comparable accuracy and resolution. The new scheme was further found to be immune to the formation of spurious vortical structures [26] that may result from under-resolution. The KT scheme was further extended to cope with other coordinate systems, and a systematic treatment of boundary conditions was derived [27].

In this work we apply the central scheme approach to viscoelastic flow. The methodology which was developed for newtonian flow is found to be naturally generalizable to more complicated equations, and in particular easily allows the inclusion of constitutive relations. With fairly modest computational effort, we are able to simulate flows which include not less than eight natural wavelengths, starting with slightly perturbed azimuthal flow and evolving for many hundreds of natural periods. In most of our calculations we used a 512×32 grid.

We now discuss the choice of constitutive equations. Our scheme is designed for differential models; this restricts our choice of equations. We consider here the Oldroyd-B constitutive equation, which provides a reasonable description of dilute solutions of flexible high-molecular-weight polymers. This equation can be derived from a molecular model where the polymers are modeled by simple Hookean springs, and it has both the newtonian fluid and the Maxwell fluid as limiting cases. In particular, it predicts no shear thinning and zero second normal stress difference. The main limitation of the Oldroyd-B equation is its prediction of unbounded extensional viscosity as the extensional strain rate exceeds some value; this drawback should not be relevant for the flows studied here. Having chosen a specific constitutive equation, we re-emphasize that the numerical scheme presented here readily generalizes to a wide class of differential constitutive equations.

The main new result of this paper is the prediction of the “natural” evolution of the secondary flow following the oscillatory instability. In the early stages, modes are independent (this is the linear regime), and there will generally exist a combination of traveling and standing waves, depending on the initial conditions. When nonlinearities enter into play, the flow decomposes into separate regions of upward- and downward-going waves. This state does not reach a limit cycle, but nonetheless can persist for a long transitory time. Eventually, the globally stable state of a periodic axially traveling wave takes over, and a stable limit cycle is reached.

The structure of this paper is as follows: In Section 2 we introduce the equations of motion. In Section 3 we describe the Couette–Taylor problem, and reformulate the equations of motion in the appropriate conservative form in axisymmetric cylindrical coordinates. In Section 4 we present the numerical scheme. We briefly review the projection method, and then describe the scheme both for interior and boundary cells. In Section 5 we review the main results of earlier work on linear and non-linear stability of Couette–Taylor flow. We then describe an alternative method to calculate the linear stability spectrum that has the advantage of being simple and easily adapted for other constitutive models. We perform stability calculations that are afterwards compared to the simulation results. In addition, we investigate the structure of the stability spectrum and find new results that generalize earlier results by Avgousti and Beris [14]. In Section 6 we present the simulation results, investigating both the stationary and the oscillatory instabilities. A discussion finally follows in Section 7.

2. THE EQUATIONS OF MOTION

The equations governing the flow of a fluid are

$$\frac{\partial \mathbf{u}}{\partial t} = -(\mathbf{u} \cdot \nabla) \mathbf{u} - \nabla p + \nabla \cdot \boldsymbol{\tau}, \quad (1)$$

where $\mathbf{u}(\mathbf{x}, t)$ is the velocity field, the scalar field $p(\mathbf{x}, t)$ is the pressure, and the tensor $\boldsymbol{\tau}(\mathbf{x}, t)$ is the state-of-stress in the fluid. Throughout this paper we assume the density of the fluid to be one. Polymeric solutions and melts are usually incompressible in which case $\mathbf{u}(\mathbf{x}, t)$ satisfies the incompressibility constraint

$$\nabla \cdot \mathbf{u} = 0. \quad (2)$$

To obtain a closed set of equations it is necessary to specify the relation between the state-of-stress and the history of the flow. Such a relation is known as a constitutive equation. In a newtonian fluid the state-of-stress depends only on the instantaneous local rate-of-strain; the extra stress is proportional to the rate-of-strain tensor,

$$\boldsymbol{\tau} = \nu_s [(\nabla \mathbf{u}) + (\nabla \mathbf{u})^\dagger] \equiv 2\nu_s \mathbf{D}, \quad (3)$$

where ν_s is the shear viscosity. This constitutive equation predicts, in particular, that the stress responds instantaneously to any deformation and has no memory; the stress vanishes as soon as the driving motion has ceased. This is not the case with a complex fluid such as a polymer solution or a polymer melt. Polymers can store elastic energy and thus contribute to the state-of-stress in the fluid even after the shearing motion has ceased. The ‘‘memory’’ of the fluid, or its elasticity, is usually characterized by a relaxation spectrum, which reflects the relaxation rates of the energy storing modes.

In the case of a dilute solution of flexible high-molecular-weight polymers the rheology is reasonably well described by the Oldroyd-B constitutive equation. In this equation the state-of-stress is separated into two components: One contribution is due to the newtonian solvent and is given by Eq. (3). The second contribution is due to the polymers and satisfies the upper-convected Maxwell equation,

$$\frac{\partial \boldsymbol{\tau}}{\partial t} = -(\mathbf{u} \cdot \nabla) \boldsymbol{\tau} + (\nabla \mathbf{u})^\dagger \cdot \boldsymbol{\tau} + \boldsymbol{\tau} \cdot (\nabla \mathbf{u}) - \frac{1}{\lambda} \boldsymbol{\tau} + 2\nu_p \mathbf{D}, \quad (4)$$

where ν_p denotes the contribution of the polymers to the shear viscosity. The Oldroyd-B equation is a two mode model; one relaxation rate is due to the solvent and is infinitely fast; the polymers are described by a single relaxation mode with relaxation time λ . This relaxation time has to be interpreted as a mean relaxation time of a realistic polymer.

It is in general difficult to establish how accurately a constitutive equation describes any particular fluid. Quantitative comparison can be carried only in very simple flows in which well defined measurements can be compared with the exact solution of the equations. Viscometric flows are a special class of fluid motions that possess a very simple deformation history; they are all kinematically equivalent to simple shear between parallel plates, except for a time-dependent rigid rotation. In a shearing flow with shear rate $\dot{\gamma}$, where the velocity is in the x -direction and its gradient is in the y -direction, one typically defines the three following viscometric functions: the viscosity, the first normal stress coefficient, and the

second normal stress coefficient. For the Oldroyd-B equation these are given respectively by

$$\begin{aligned} v &\equiv \frac{\tau^{xy}}{\gamma} = v_s + v_p, \\ \Psi_1 &\equiv \frac{\tau^{xx} - \tau^{yy}}{\gamma^2} = 2\lambda v_p, \end{aligned} \quad (5)$$

and

$$\Psi_2 \equiv \frac{\tau^{yy} - \tau^{zz}}{\gamma^2} = 0.$$

In particular the Oldroyd-B equation predicts that the shear viscosity does not depend on the shear rate (no shear thinning).

3. THE COUETTE–TAYLOR PROBLEM

A circular Couette cell consists of two concentrically rotating cylinders between which the fluid is confined. We consider a viscoelastic fluid described by the Oldroyd-B constitutive equation in such a geometry. We restrict ourselves here to axisymmetric flow; the velocity field and the stress components do not depend on the azimuthal coordinate. Experiments indicate that flow is indeed axisymmetric for ranges of parameters close enough to the primary instability threshold.

The geometry suggests the natural choice of cylindrical coordinates; let $\mathbf{x} = (r, \theta, z)$ denote the radial, azimuthal, and axial coordinates, respectively. The corresponding components of the velocity field and the stress tensor are denoted by $\mathbf{u} = (u, v, w)$ and $\boldsymbol{\tau} = [(\tau^{rr}, \tau^{r\theta}, \tau^{rz}), (\tau^{\theta r}, \tau^{\theta\theta}, \tau^{\theta z}), (\tau^{zr}, \tau^{z\theta}, \tau^{zz})]$. The stress tensor is always symmetric; therefore it only has six independent components.

We now write the equations of motion in cylindrical coordinates. The central scheme described in the next section is based on the dual nature of the equations, which can be formulated both in advective form (1), (4) and in (partially) conservative form; the advective operator $\partial f / \partial t + (\mathbf{u} \cdot \nabla) f$ can be replaced by the conservative operator $\partial f / \partial t + \nabla \cdot (\mathbf{u} f)$ for any scalar function f . The equivalence of the two representation is guaranteed by the incompressibility condition (2).

It is a matter of straightforward algebra to write Eq. (1) in cylindrical coordinates assuming azimuthal symmetry in the appropriate conservative form,

$$\begin{aligned} \frac{\partial u}{\partial t} &= \frac{1}{r} \frac{\partial}{\partial r} r \left[-u^2 + v_s \frac{\partial u}{\partial r} + \tau^{rr} \right] + \frac{\partial}{\partial z} \left[-wu + v_s \frac{\partial u}{\partial z} + \tau^{rz} \right] \\ &\quad + \left[\frac{v^2}{r} - \frac{\partial p}{\partial r} - v_s \frac{u}{r^2} - \frac{1}{r} \tau^{\theta\theta} \right], \\ \frac{\partial v}{\partial t} &= \frac{1}{r} \frac{\partial}{\partial r} r \left[-uv + v_s \frac{\partial v}{\partial r} + \tau^{r\theta} \right] + \frac{\partial}{\partial z} \left[-wv + v_s \frac{\partial v}{\partial z} + \tau^{\theta z} \right] \\ &\quad + \left[-\frac{vu}{r} - v_s \frac{v}{r^2} + \frac{1}{r} \tau^{r\theta} \right], \\ \frac{\partial w}{\partial t} &= \frac{1}{r} \frac{\partial}{\partial r} r \left[-uw + v_s \frac{\partial w}{\partial r} + \tau^{rz} \right] + \frac{\partial}{\partial z} \left[-w^2 + v_s \frac{\partial w}{\partial z} + \tau^{zz} \right] + \left[-\frac{\partial p}{\partial z} \right], \end{aligned} \quad (6)$$

where the newtonian viscosity has been included explicitly, while τ now represents only the polymer contribution to the state-of-stress. The incompressibility condition in cylindrical coordinates reads

$$\frac{1}{r} \frac{\partial}{\partial r}(ru) + \frac{\partial w}{\partial z} = 0. \quad (7)$$

The equations for the six independent components of the stress tensor are

$$\begin{aligned} \frac{\partial \tau^{rr}}{\partial t} &= \frac{1}{r} \frac{\partial}{\partial r} r[-u\tau^{rr}] + \frac{\partial}{\partial z}[-w\tau^{rr}] + \left[2 \frac{\partial u}{\partial z} \tau^{rz} + 2 \frac{\partial u}{\partial r} \tau^{rr} \right] - \frac{1}{\lambda} \tau^{rr} + 2 \frac{v_p}{\lambda} \frac{\partial u}{\partial r}, \\ \frac{\partial \tau^{\theta\theta}}{\partial t} &= \frac{1}{r} \frac{\partial}{\partial r} r[-u\tau^{\theta\theta}] + \frac{\partial}{\partial z}[-w\tau^{\theta\theta}] + \left[\frac{\partial u}{\partial z} \tau^{\theta z} + \frac{\partial v}{\partial z} \tau^{rz} + \frac{\partial u}{\partial r} \tau^{r\theta} + \frac{\partial v}{\partial r} \tau^{rr} \right] \\ &\quad + \frac{1}{r} [u\tau^{r\theta} - v\tau^{rr}] - \frac{1}{\lambda} \tau^{\theta\theta} + \frac{v_p}{\lambda} \left[\frac{\partial v}{\partial r} - \frac{v}{r} \right], \\ \frac{\partial \tau^{rz}}{\partial t} &= \frac{1}{r} \frac{\partial}{\partial r} r[-u\tau^{rz}] + \frac{\partial}{\partial z}[-w\tau^{rz}] + \left[\frac{\partial u}{\partial z} \tau^{zz} + \frac{\partial w}{\partial r} \tau^{rr} \right] - \frac{1}{\lambda} \tau^{rz} + \frac{v_p}{\lambda} \left[\frac{\partial u}{\partial z} + \frac{\partial w}{\partial r} \right], \\ \frac{\partial \tau^{\theta\theta}}{\partial t} &= \frac{1}{r} \frac{\partial}{\partial r} r[-u\tau^{\theta\theta}] + \frac{\partial}{\partial z}[-w\tau^{\theta\theta}] + \left[2 \frac{\partial v}{\partial z} \tau^{\theta z} + 2 \frac{\partial v}{\partial r} \tau^{r\theta} \right] + \frac{2}{r} [u\tau^{\theta\theta} - v\tau^{r\theta}] \quad (8) \\ &\quad - \frac{1}{\lambda} \tau^{\theta\theta} + 2 \frac{v_p}{\lambda} \frac{u}{r}, \\ \frac{\partial \tau^{\theta z}}{\partial t} &= \frac{1}{r} \frac{\partial}{\partial r} r[-u\tau^{\theta z}] + \frac{\partial}{\partial z}[-w\tau^{\theta z}] + \left[\frac{\partial v}{\partial z} \tau^{zz} + \frac{\partial w}{\partial z} \tau^{\theta z} + \frac{\partial v}{\partial r} \tau^{rz} + \frac{\partial w}{\partial r} \tau^{r\theta} \right] \\ &\quad + \frac{1}{r} [u\tau^{\theta z} - v\tau^{rz}] - \frac{1}{\lambda} \tau^{\theta z} + \frac{v_p}{\lambda} \frac{\partial v}{\partial z}, \\ \frac{\partial \tau^{zz}}{\partial t} &= \frac{1}{r} \frac{\partial}{\partial r} r[-u\tau^{zz}] + \frac{\partial}{\partial z}[-w\tau^{zz}] + \left[2 \frac{\partial w}{\partial z} \tau^{zz} + 2 \frac{\partial w}{\partial r} \tau^{rz} \right] - \frac{1}{\lambda} \tau^{zz} + 2 \frac{v_p}{\lambda} \frac{\partial w}{\partial z}. \end{aligned}$$

We next specify the boundary conditions. Let R_{in} and R_{out} denote the radii of the inner and outer cylinders, respectively. The no-slip conditions imply that the velocity of the fluid at the walls equals the velocity of the cylinders, namely

$$\begin{aligned} u(R_{in}) &= u(R_{out}) = w(R_{in}) = w(R_{out}) = 0, \\ v(R_{in}) &= \Omega_{in} R_{in}, \quad v(R_{out}) = \Omega_{out} R_{out}. \end{aligned} \quad (9)$$

In the axial direction we will use periodic boundary conditions for convenience. This choice has reasonably little effect on the flow as long as the height of the cylinders is large compared to the wavelength of the flow pattern.

The number of independent parameters can be reduced by the introduction of dimensionless variables. For that one has to pick suitable length and time scales. We will measure length in units of the intercylindrical gap, $R_{out} - R_{in}$, and time in units of the inner cylinder rotation period, $1/\Omega_{in}$. The velocity is then expressed in units of $\Omega_{in}(R_{out} - R_{in})$, the stress

in units of $\Omega_{in}^2(R_{out} - R_{in})^2$, and the viscosity in units of $\Omega_{in}(R_{out} - R_{in})^2$. In these units the boundary conditions for the azimuthal velocity are

$$v(r_L) = r_L, \quad v(r_R) = \omega r_R, \quad (10)$$

where

$$r_L = \frac{\eta}{1 - \eta}, \quad r_R = \frac{1}{1 - \eta} \quad (11)$$

denote the cylindrical radii, $\eta \equiv R_{in}/R_{out}$, and $\omega \equiv \Omega_{out}/\Omega_{in}$. Thus the model includes a total of five independent parameters: η , ω , v_s , v_p , and λ .

For all values of the parameters the model defined by Eqs. (6), (7), and (8) and subject to the boundary conditions (10) has a viscometric solution,

$$\begin{aligned} u_0 &= w_0 = 0, \\ v_0(r) &= Ar + \frac{B}{r}, \end{aligned} \quad (12)$$

where the coefficients A and B are given by

$$A = \frac{\omega - \eta^2}{1 - \eta^2}, \quad B = \frac{(1 - \omega)\eta^2}{(1 - \eta)^2(1 - \eta^2)}, \quad (13)$$

and

$$\begin{aligned} \tau_0^{rr} &= \tau_0^{rz} = \tau_0^{\theta z} = \tau_0^{zz} = 0 \\ \tau_0^{r\theta}(r) &= -\frac{2Bv_p}{r^2} \\ \tau_0^{\theta\theta}(r) &= \frac{8B^2\lambda v_p}{r^4}. \end{aligned} \quad (14)$$

4. THE NUMERICAL SCHEME

In axisymmetric flow the velocity field and the stress tensor depend only on the radial coordinate, r , and the axial coordinate, z . The computational grid consists of rectangular cells of size $\Delta r \times \Delta z$; at time t^n these cells $\mathbb{C}_{i,j}$ are centered at $(r_i = r_L + i\Delta r, z_j = j\Delta z)$, with $i = 0, \dots, M - 1$ and $j = 0, \dots, N - 1$.

A numerical scheme is a recipe which specifies how to calculate discrete data at time t^{n+1} given data at time t^n . We assume as initial data the *point values* of the three velocity components and the six stress components at the *centers* of the computational cells $\mathbb{C}_{i,j}$; they are denoted by $(u_{i,j}^n, v_{i,j}^n, w_{i,j}^n)$ and $[(\tau^{rr})_{i,j}^n, (\tau^{rz})_{i,j}^n, (\tau^{r\theta})_{i,j}^n, (\tau^{\theta\theta})_{i,j}^n, (\tau^{\theta z})_{i,j}^n, (\tau^{zz})_{i,j}^n]$, respectively. For compactness we define a nine-component vector field, $\psi(\mathbf{x}, t)$, which contains the components of the velocity field and the stress tensor; the initial condition is thus defined by the specification of $\psi_{i,j}^n$. The pressure gradient is also assumed to be given at the centers of the cells $\mathbb{C}_{i,j}$, but at the former mid-time $t^{n-1/2}$; its r - and z -components are denoted by $\nabla_r p_{i,j}^{n-1/2}$ and $\nabla_z p_{i,j}^{n-1/2}$.

4.1. The Projection Method

The solution represented by the vector $\boldsymbol{\psi}(\mathbf{x}, t)$ has to be evolved in time from t^n to t^{n+1} . The flow equations are given by Eqs. (6) and (8), subject to the elliptic incompressibility constraint imposed by Eq. (7). This constraint determines the pressure $p(\mathbf{x}, t)$, which can be viewed as a Lagrange multiplier.

We follow the projection method [24]. To illustrate the basic idea, consider the following second-order temporal discretization of the equations of motion for the velocity field,

$$\frac{\mathbf{u}^{n+1} - \mathbf{u}^n}{\Delta t} = [-(\mathbf{u} \cdot \nabla)\mathbf{u} + \nu_s \nabla^2 \mathbf{u} + \nabla \cdot \boldsymbol{\tau}]^{n+1/2} - \nabla p^{n+1/2}, \quad (15)$$

where the updated flow field has to satisfy the incompressibility condition

$$\nabla \cdot \mathbf{u}^{n+1} = 0. \quad (16)$$

Ignoring momentarily the evolution of the stress tensor, Eqs. (15) and (16) form together a set of equations for the unknowns \mathbf{u}^{n+1} and $\nabla p^{n+1/2}$. The problem is how to evolve the velocity field in time, while satisfying the elliptic constraint all along the time evolution.

If $\nabla p^{n+1/2}$ is replaced in Eq. (15) by the value at the former mid-point, $\nabla p^{n-1/2}$, then one gets, instead of the actual updated field, a provisional field,

$$\mathbf{u}^* = \mathbf{u}^n + \Delta t [-(\mathbf{u} \cdot \nabla)\mathbf{u} + \nu_s \nabla^2 \mathbf{u} + \nabla \cdot \boldsymbol{\tau}]^{n+1/2} - \Delta t \nabla p^{n-1/2}. \quad (17)$$

The key to the projection method is the fact that, to second-order accuracy, \mathbf{u}^* differs from \mathbf{u}^{n+1} by the gradient of a scalar function that equals approximately $\Delta t (\nabla p^{n+1/2} - \nabla p^{n-1/2})$. The Hodge decomposition theorem states that any vector field \mathbf{u} can be uniquely decomposed into a divergence-free field, which is tangential to the domain boundaries and an irrotational, or gradient, field; the space of divergence-free vector fields and the space of vector fields that are gradients of scalar fields are orthogonal and complementary. In other words, given the provisional field \mathbf{u}^* , its decomposition into the updated flow field \mathbf{u}^{n+1} and the residual gradient is well-posed and unique.

Let \mathbb{P} denote the operator that projects a vector field onto the space of divergence-free vector fields. Then Eqs. (15) and (16) can be replaced by the equivalent set of equations,

$$\mathbf{u}^{n+1} = \mathbb{P} \mathbf{u}^* \quad (18)$$

and

$$\nabla p^{n+1/2} = \nabla p^{n-1/2} + \frac{1}{\Delta t} (\mathbb{I} - \mathbb{P}) \mathbf{u}^*, \quad (19)$$

where \mathbb{I} is the identity operator.

4.2. Interior Cells

4.2.1. Piecewise-Linear Reconstruction

The initial data at time t^n provides only partial information about the state of the system; it includes only values at discrete grid points. The first step in many numerical schemes is an approximate reconstruction of the fields to recover point values throughout the domain.

A particular choice of reconstruction is by a piecewise-polynomial function; for second-order accuracy we need a piecewise-linear approximant, which takes the form

$$\psi^n(r, z) = \psi_{i,j}^n + \psi'_{i,j}(r - r_i) + \psi_{i,j}(z - z_j), \quad r, z \in \mathbb{C}_{i,j}, \quad (20)$$

where the discrete fields $\psi'_{i,j}$ and $\psi_{i,j}$ approximate the r - and z -derivatives of $\psi^n(r, z)$ at the centers of the cells $\mathbb{C}_{i,j}$. In general the recipe for constructing such numerical derivatives requires nonlinear limiters in order to prevent the formation of nonlinear oscillations [28–31]. As reported in [23], our scheme proves to be robust against the formation and the propagation of such oscillations. We can therefore approximate $\psi'_{i,j}$ and $\psi_{i,j}$ by simple central differences,

$$\psi'_{i,j} = D_r^0 \psi_{i,j}^n, \quad \psi_{i,j} = D_z^0 \psi_{i,j}^n, \quad (21)$$

where D_r^0 and D_z^0 denote the r - and z -central difference operators.

4.2.2. Calculation of $\psi_{i+1/2,j+1/2}^{n+1}$

As explained above, the projection method allows us to consider the evolution of the velocity field by substituting for the pressure field its value at the former time step. The actual velocity field can be recovered from the provisional field at the end of the procedure. Thus we can now describe the part of the scheme which performs the time integration.

The equations of motion, (6) and (8), have been formulated in conservative form; they can be written as a system of equations of the general form

$$\frac{\partial \psi}{\partial t} = \frac{1}{r} \frac{\partial}{\partial r} r \mathbf{F}(\psi, r) + \frac{\partial}{\partial z} \mathbf{G}(\psi, r) + \mathbf{S}(\psi, r), \quad (22)$$

where $\psi(\mathbf{x}, t)$ again denotes the vector (\mathbf{u}, τ) . The vector functions $\mathbf{F}(\psi, r)$ and $\mathbf{G}(\psi, r)$ are the r - and z -components of the corresponding fluxes, and the vector function $\mathbf{S}(\psi, r)$ is a source which includes all those terms that do not fit into conservation form.

Given the initial data $\psi_{i,j}^n$, we evolve it to time t^{n+1} and calculate its cell averages, $\bar{\psi}_{i+1/2,j+1/2}^{n+1}$, over the *staggered-grid* cells, $\mathbb{C}_{i+1/2,j+1/2}$. Note that averages in cylindrical coordinates have to be weighted proportionally to the radius. These cell averages can be represented as integrals over the control box, $\mathbb{C}_{i+1/2,j+1/2} \times [t^n, t^{n+1}]$,

$$\begin{aligned} \bar{\psi}_{i+1/2,j+1/2}^{n+1} &= \int_{\mathbb{C}_{i+1/2,j+1/2}} r \, dr \, dz \, \psi^{n+1}(r, z) \\ &= \int_{\mathbb{C}_{i+1/2,j+1/2}} r \, dr \, dz \, \psi^n(r, z) + \int_{t^n}^{t^{n+1}} dt \int_{\mathbb{C}_{i+1/2,j+1/2}} r \, dr \, dz \, \frac{\partial \psi}{\partial t}. \end{aligned} \quad (23)$$

The computational grid and the control box are sketched in Fig. 1. The notation $f_{\Omega} = (1/\Omega) \int_{\Omega}$ is for normalized integrals, scaled by their area, length, etc. For example, the volume of the annulus whose cross section is the staggered-grid cell $\mathbb{C}_{i+1/2,j+1/2}$ is $r_{i+1/2} \Delta r \Delta z$.

The first term in Eq. (23) is just an average over the piecewise-linear approximant, $\psi^n(r, z)$, over the bottom of the control box shown in Fig. 1. It is a sum over contributions arising from the four intersecting cells, $\mathbb{C}_{i,j}$, $\mathbb{C}_{i+1,j}$, $\mathbb{C}_{i,j+1}$, and $\mathbb{C}_{i+1,j+1}$. A straightforward

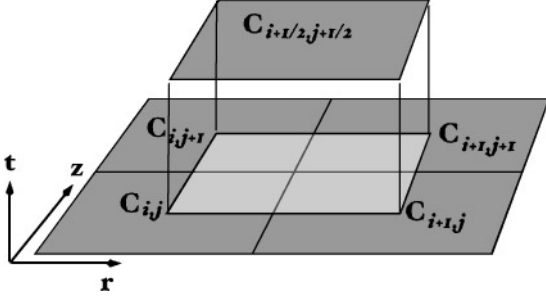


FIG. 1. The computational grid: At time t^n the data is given at the centers of the grid cells $\mathbb{C}_{i,j}$, ($i\Delta r$, $j\Delta z$). At time t^{n+1} a staggered grid with cells $\mathbb{C}_{i+1/2,j+1/2}$ is used.

computation gives

$$\begin{aligned} \int_{\mathbb{C}_{i+1/2,j+1/2}} d\mathbf{x} \psi^n &= \mu_r^+ \mu_z^+ \psi_{i,j}^n + \frac{\Delta r^2}{8r_{i+1/2}} D_r^+ \mu_z^+ \psi_{i,j}^n - \frac{\Delta r^2}{8} D_r^+ \mu_z^+ \psi'_{i,j} \\ &\quad - \frac{\Delta r^2}{24r_{i+1/2}} \mu_r^+ \mu_z^+ \psi'_{i,j} - \frac{\Delta z^2}{8} D_z^+ \mu_r^+ \psi'_{i,j}. \end{aligned} \quad (24)$$

We have introduced the discrete operators $D_r^+ \psi_{i..} \equiv (\psi_{i+1..} - \psi_{i..})/\Delta r$ and $\mu_r^+ \psi_{i..} \equiv \frac{1}{2}(\psi_{i+1..} + \psi_{i..})$ which denote forward differences and forward averages in the r direction, respectively. The meaning of the related operators D_r^- , μ_r^- , D_z^+ , D_z^- , μ_z^+ , and μ_z^- is self-evident.

In the second term of equation (23) $\partial\psi/\partial t$ is replaced by the equation of motion (22); i.e., the divergence of the flux and the source are integrated over the control box. It is in the integration over the fluxes $\mathbf{F}(\psi, r)$ and $\mathbf{G}(\psi, r)$ that the virtues of the conservation form enter. For example, the integral $\int r dr$ over $(1/r)(\partial/\partial r)r\mathbf{F}$ is simple to perform and equals the flux difference between r_{i+1} and r_i . This flux difference is then integrated over the two interfaces of the control box (Fig. 2),

$$\begin{aligned} &\int_{t_n}^{t_{n+1}} dt \int_{\mathbb{C}_{i+1/2,j+1/2}} r dr dz \frac{1}{r} \frac{\partial}{\partial r} r \mathbf{F}(\psi(r, z, t), r) \\ &= \frac{1}{r_{i+1/2}} D_r^+ \int_{t_n}^{t_{n+1}} dt \int_{J_{j+1/2}} dz r_i \mathbf{F}(\psi(r_i, z, t), r_i), \end{aligned} \quad (25)$$

where $J_{j+1/2}$ refers to the segment of length Δz centered at $z_{j+1/2}$.

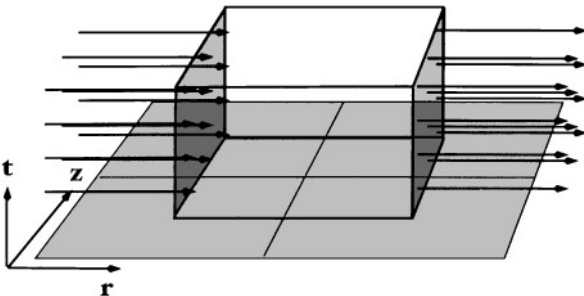


FIG. 2. Illustration of the integration over the flux: The integral over the control box $\mathbb{C}_{i+1/2,j+1/2} \times [t^n, t^{n+1}]$ reduces to the flux difference integrated over the sides normal to the flux (shaded areas).

So far, the procedure is exact. Approximations are required in order to integrate $(r\mathbf{F})$ over the interfaces of the control box. For second-order accuracy, the integral over z can be approximated by the second-order trapezoidal rule. The integral over time is approximated by the mid-point rule. For that, we need an estimate of the fields at time $t^{n+1/2}$ at the centers of the cells $\mathbb{C}_{i,j}$; $\psi_{i,j}^{n+1/2}$ can be obtained by a first-order explicit predictor step.

The integration over the flux \mathbf{G} follows the same lines. There remains the source term $\mathbf{S}(\psi, r)$ for which the spatial integration can be approximated by a second-order averaging over the four corners,

$$\int_{\mathbb{C}_{i+1/2,j+1/2}} r dr dz \mathbf{S}(\psi(r, z, t), r) \simeq \frac{1}{r_{i+1/2}} \mu_r^+ \mu_z^+ [r \mathbf{S}(\psi(r_i, z_j, t), r_i)]. \quad (26)$$

The time integration is again approximated by the mid-point rule.

Thus the calculation of the cell-averages $\bar{\psi}_{i+1/2,j+1/2}^{n+1}$ consists of a predictor step for which one can use a simple forward Euler scheme. For example, the predicted value of the radial velocity component is

$$\begin{aligned} u_{i,j}^{n+1/2} = & u_{i,j}^n + \frac{\Delta t}{2} \left\{ -u_{i,j}^n u'_{i,j} - w_{i,j}^n u'_{i,j} + \frac{(v_{i,j}^n)^2}{r_i} - \nabla_r p_{i,j}^{n-1/2} + v_s \left(\frac{u'_{i,j}}{r_i} - \frac{u_{i,j}^n}{r_i^2} \right) \right. \\ & \left. + v_s \left(\frac{\partial^2 u_{i,j}^n}{\partial r^2} + \frac{\partial^2 u_{i,j}^n}{\partial z^2} \right) + (\tau^{rr})'_{i,j} + (\tau^{rz})'_{i,j} + \frac{(\tau^{rr})_{i,j}^n - (\tau^{\theta\theta})_{i,j}^n}{r_i} \right\}. \quad (27) \end{aligned}$$

The predictor step is followed by a corrector,

$$\begin{aligned} \bar{\psi}_{i+1/2,j+1/2}^{n+1} = & \mu_r^+ \mu_z^+ \psi_{i,j}^n + \frac{\Delta r^2}{8r_{i+1/2}} D_r^+ \mu_z^+ \psi_{i,j}^n - \frac{\Delta r^2}{8} D_r^+ \mu_z^+ \psi'_{i,j} \\ & - \frac{\Delta r^2}{24r_{i+1/2}} \mu_r^+ \mu_z^+ \psi'_{i,j} - \frac{\Delta z^2}{8} D_z^+ \mu_r^+ \psi'_{i,j} \\ & + \frac{\Delta t}{r_{i+1/2}} D_r^+ \mu_z^+ \{r_i \mathbf{F}(\psi_{i,j}^{n+1/2}, r_i)\} \\ & + \frac{\Delta t}{r_{i+1/2}} D_z^+ \mu_r^+ \{r_i \mathbf{G}(\psi_{i,j}^{n+1/2}, r_i)\} \\ & + \frac{\Delta t}{r_{i+1/2}} \mu_r^+ \mu_z^+ \{r_i \mathbf{S}(\psi_{i,j}^{n+1/2}, r_i)\}. \quad (28) \end{aligned}$$

Once we have obtained the cell averages $\bar{\psi}_{i+1/2,j+1/2}^{n+1}$ (recalling, however, that the velocity field is just provisional), we need to recover back the point values $\psi_{i+1/2,j+1/2}^{n+1}$ at the centers of the staggered-grid cells $\mathbb{C}_{i+1/2,j+1/2}$. If the field $\psi^{n+1}(r, z)$ is approximated to leading order by a piecewise-linear function,

$$\begin{aligned} \psi^{n+1}(r, z) = & \psi_{i+1/2,j+1/2}^{n+1} + (\psi^{n+1})'_{i+1/2,j+1/2} (r - r_{i+1/2}) \\ & + (\psi^{n+1})'_{i+1/2,j+1/2} (z - z_{j+1/2}), \quad (29) \end{aligned}$$

for $(r, z) \in \mathbb{C}_{i+1/2,j+1/2}$, then its cell averages are given by

$$\bar{\psi}_{i+1/2,j+1/2}^{n+1} = \psi_{i+1/2,j+1/2}^{n+1} + \frac{\Delta r^2}{12r_{i+1/2}} (\psi^{n+1})'_{i+1/2,j+1/2}. \quad (30)$$

It is sufficient, within second-order accuracy, to replace $(\psi^{n+1})'_{i+1/2,j+1/2}$ by $(\bar{\psi}^{n+1})'_{i+1/2,j+1/2}$, where the latter is evaluated by central differencing. Thus the point values are recovered from the cell averages by

$$\psi_{i+1/2,j+1/2}^{n+1} = \bar{\psi}_{i+1/2,j+1/2}^{n+1} - \frac{\Delta r^2}{12r_{i+1/2}} D_r^0 \bar{\psi}_{i+1/2,j+1/2}^{n+1}. \quad (31)$$

A slightly different procedure is adopted for the temporal integration of the parabolic terms, i.e., the newtonian viscosity, in the equations for the velocity field. Stability considerations favor the use of the implicit Crank–Nicholson scheme, rather than the explicit predictor–corrector scheme. See [23, 27] for more details.

This concludes the calculation of the provisional field $\mathbf{u}_{i+1/2,j+1/2}^*$ and the updated stress tensor $\tau_{i+1/2,j+1/2}^{n+1}$.

4.2.3. Hodge Projection

In the previous section we calculated the nondivergence-free provisional field \mathbf{u}^* . The last step in the scheme accounts for incompressibility by extracting from \mathbf{u}^* its divergence-free part. The remainder (irrotational) part is needed to update the pressure gradient.

In the continuum limit, the updated flow field \mathbf{u}^{n+1} needs to satisfy the incompressibility condition

$$\frac{1}{r} \frac{\partial}{\partial r} (r u^{n+1}) + \frac{\partial w^{n+1}}{\partial z} = 0. \quad (32)$$

Because the central differencing approach is based on cell averaging, it is more appropriate to impose the incompressibility condition in its integral form. Integrating (32) over the cell $\mathbb{C}_{i,j}$ we get

$$\Delta r D_r^- \int_{j_j} dz r_{i+1/2} u_{i+1/2,j+1/2}^{n+1} + \Delta z D_z^- \int_{I_i} dz r_{i+1/2} w_{i+1/2,j+1/2}^{n+1} = 0 \quad (33)$$

which is again approximated with the second-order trapezoidal rule. Thus the discrete form of the incompressibility condition is

$$D_r^- \mu_z^- (r_{i+1/2} u_{i+1/2,j+1/2}^{n+1}) + D_z^- \mu_r^- (r_{i+1/2} w_{i+1/2,j+1/2}^{n+1}) = 0. \quad (34)$$

We now perform a discrete Hodge decomposition. We decompose the provisional field $\mathbf{u}_{i+1/2,j+1/2}^*$ into the sum of the updated flow field $\mathbf{u}_{i+1/2,j+1/2}^{n+1}$ and the gradient of a yet unknown scalar grid function $\phi_{i,j}$,

$$\begin{aligned} u_{i+1/2,j+1/2}^* &= u_{i+1/2,j+1/2}^{n+1} + D_r^+ \mu_z^+ \phi_{i,j} \\ v_{i+1/2,j+1/2}^* &= v_{i+1/2,j+1/2}^{n+1} \\ w_{i+1/2,j+1/2}^* &= w_{i+1/2,j+1/2}^{n+1} + D_z^+ \mu_r^+ \phi_{i,j}. \end{aligned} \quad (35)$$

Up to the specification of boundary conditions (which are discussed in the next section), the substitution of the decomposition (35) into the discrete incompressibility condition (34) dictates the scalar potential $\phi_{i,j}$. It is the solution of the Poisson equation,

$$\mu_z^+ \mu_z^- D_r^- (r_{i+1/2} D_r^+ \phi_{i,j}) + D_z^+ D_z^- \mu_r^- (r_{i+1/2} \mu_r^+ \phi_{i,j}) = \rho_{i,j}, \quad (36)$$

where

$$\rho_{i,j} = D_r^- \mu_z^- (r_{i+1/2} w_{i+1/2,j+1/2}^*) + D_z^- \mu_r^- (r_{i+1/2} w_{i+1/2,j+1/2}^*). \quad (37)$$

The calculation of $\phi_{i,j}$ allows the flow field to be updated from Eq. (35), and the pressure gradient is updated by

$$\begin{aligned} \nabla_r p_{i+1/2,j+1/2}^{n+1/2} &= \mu_r^+ \mu_z^+ \nabla_r p_{i,j}^{n-1/2} + \frac{1}{\Delta t} D_r^+ \mu_z^+ \phi_{i,j} \\ \nabla_z p_{i+1/2,j+1/2}^{n+1/2} &= \mu_r^+ \mu_z^+ \nabla_z p_{i,j}^{n-1/2} + \frac{1}{\Delta t} D_z^+ \mu_r^+ \phi_{i,j}. \end{aligned} \quad (38)$$

This concludes the calculation of one time step.

The evolution of the flow field from time t^n to time t^{n+1} induces a spatial shift from the cells $\mathbb{C}_{i,j}$ to the staggered-grid cells $\mathbb{C}_{i+1/2,j+1/2}$. If repeated, this procedure would lead to a continual drift of the computational domain. In order to prevent this from happening, the scheme alternates, back and forth, between the two grids. Thus after a time step that shifts from the grid $\mathbb{C}_{i,j}$ to the grid $\mathbb{C}_{i+1/2,j+1/2}$, the next time step reverts back to the original grid. The calculations involved in the alternating steps are identical, up to a systematic interchange between forward and backward operators (e.g., $D_r^+ \leftrightarrow D_r^-$), and between the coordinates of the cell centers, $(r_i, z_j) \leftrightarrow (r_{i+1/2}, z_{j+1/2})$.

4.3. Boundary Cells

4.3.1. Grid Structure

The numerical scheme remains to be adapted for boundary cells; as we are using periodic boundary conditions that concern is only for the radial boundary cells, $(0, j)$ and $(M-1, j)$. The alternation between two grids requires special attention; if, for example, the right boundary cells are entirely inside the physical domain at the end of the n th time step (i.e., the right boundaries of the cells coincide with the right wall), then the right boundary cells will be intersected by the wall at the end of the subsequent time step.

We first need to specify the structure of the computational grid and, notably, its location with respect to the domain boundaries. We adopt the following convention: In the initial state, the left edge of the system ($r = r_L$) intersects the left boundary cells (i.e., $r_0 = r_L$), while the right edge of the system ($r = r_R$) coincides with the edge of the right boundary cells (i.e., $r_{M-1} = r_R - \frac{1}{2} \Delta r$). That is, the right boundary cells lie entirely inside the system, whereas only half of the left boundary cells do so. This situation is reversed in the succeeding time step. This structure is illustrated in Fig. 3. This structure determines in particular the grid spacing: for the radial axis, $\Delta r = (r_R - r_L)/(M - \frac{1}{2})$; for the axial axis, $\Delta z = h/N$, where h denotes the height of the cylinders.

As in the preceding section, we will describe the procedure only for time steps which start with the grid $\mathbb{C}_{i,j}$ and end with the staggered grid $\mathbb{C}_{i+1/2,j+1/2}$.

4.3.2. Piecewise-Linear Reconstruction

The piecewise-linear approximant $\psi^n(r, z)$ assumes the same form (20) inside the boundary cells. The only modification is in the calculation of the r -derivatives, which have to use

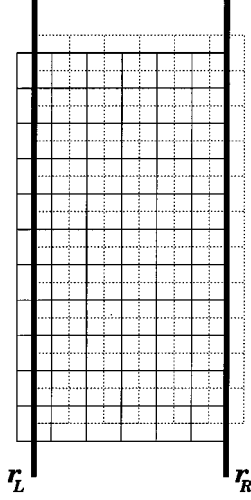


FIG. 3. Sketch of the computational grid and the physical domain. The data are given at the centers of the solid grid cells at the beginning of the odd time steps. The left boundary cells are intersected by the left wall, whereas the right boundary cells are entirely inside the domain. The situation is reversed at the beginning of the even time steps where the data are given at the centers of the dotted grid cells.

second-order one-sided expressions,

$$\begin{aligned}\psi'_{0,..} &= -\frac{1}{2h}(3\psi_{0,..}^n - 4\psi_{1,..}^n + \psi_{2,..}^n) \\ \psi'_{M-1,..} &= \frac{1}{2h}(3\psi_{M-1,..}^n - 4\psi_{M-2,..}^n - \psi_{M-3,..}^n).\end{aligned}\quad (39)$$

4.3.3. Calculation of $\psi_{i+1/2,j+1/2}^{n+1}$

As described in Section 3.1.2, the calculation of the updated field, $\psi_{i+1/2,j+1/2}^{n+1}$ consists of three steps: (i) a predictor to estimate $\psi_{i,j}^{n+1/2}$; (ii) a corrector to calculate cell averages $\bar{\psi}_{i+1/2,j+1/2}^{n+1}$; and (iii) an interpolation which recovers the point values $\psi_{i+1/2,j+1/2}^{n+1}$.

The predictor $\psi_{i,j}^{n+1/2}$ has to be calculated at the centers of the cells $\mathbb{C}_{i,j}$. The right boundary cells ($i = M - 1$) lie entirely inside the system and, therefore, can follow exactly the same treatment (27) as interior cells, with the derivative operators replaced by one-sided stencils. The centers of the left boundary cells lie, on the other hand, on the left wall. The values of the velocity components are determined at these points by the boundary conditions, hence we set $\mathbf{u}_{0,..}^{n+1/2} = \mathbf{u}(r_L)$.

The treatment of the stress components at the left boundary cells is substantially different. The characteristics of the stress are advected by the velocity field; since the normal velocity vanishes at the walls, characteristics do not enter into the system, and one is not allowed to impose boundary conditions on the stress tensor. In principle one has to derive the discrete evolution equations appropriate for these half-cells. A simple alternative is to evaluate the stress at the wall with a second-order extrapolation based on values of the stress in the interior.

In the corrector step this picture repeats itself, except for an exchange of role between left and right. This time the left boundary cells can be treated as interior cells, while $\mathbf{u}_{M-1,..}^* = \mathbf{u}(r_R)$, and $\tau_{i+1/2,j+1/2}^{n+1}$ is evaluated at the right wall by a suitable extrapolation.

4.3.4. Hodge Projection

The Hodge projection (35) decomposes the provisional field \mathbf{u}^* into a divergence-free field \mathbf{u}^{n+1} and an irrotational field. In the continuum case, only the normal component of the divergence-free part can be specified, $u^{n+1}(r_L) = u^{n+1}(r_R) = 0$. In the discrete formulation it is possible within second-order accuracy to impose constraints also on the tangential component w^{n+1} .

The vector fields \mathbf{u}^* and \mathbf{u}^{n+1} are specified at the centers of the staggered-grid cells $\mathbb{C}_{i+1/2, j+1/2}$, whereas the scalar field $\phi_{i,j}$ is given at the centers of the original cells $\mathbb{C}_{i,j}$. At the left boundary ($i = 0$) the gradient of ϕ can be calculated using the same differencing stencil as in the interior cells. Because the flow field is not specified at the boundary, we will require that the *extrapolated* value of u^{n+1} vanish at $r = r_L$, i.e.,

$$\frac{1}{8}\mu_z^+ (15u_{1/2, \cdot}^{n+1} - 10u_{3/2, \cdot}^{n+1} + 3u_{5/2, \cdot}^{n+1}) = 0. \quad (40)$$

On the right side ($i = M - 1$) the flow field is calculated at the boundary. The fact that both $u_{i+1/2, j+1/2}^{n+1}$ and $w_{i+1/2, j+1/2}^{n+1}$ vanish at those points determines the form of the incompressibility condition with respect to the boundary cells $\mathbb{C}_{i,j}$,

$$-\frac{1}{\Delta r}\mu_z^+\mu_z^-D_r^-\phi_{i,j} + \frac{1}{2}D_z^+D_z^-\mu_r^-\phi_{i,j} = -\frac{1}{\Delta r}\mu_z^-u_{i-1/2, j+1/2}^* + \frac{1}{2}D_z^-w_{i-1/2, j+1/2}^*. \quad (41)$$

Equations (40) and (41) complete the specification of the boundary conditions for $\phi_{i,j}$.

We note that the Poisson equation defined by Eqs. (36), (40), and (41) has a two-dimensional null space which corresponds to two additive constants, one for each of two decoupled stencils (“checkerboard” pattern). These two degrees of freedom do not affect the values of the updated fields and therefore can be set arbitrarily.

4.4. Time Step Selection

The equations of motion (1) and (4) form a hyperbolic system of nine equations, if we momentarily ignore the newtonian viscosity, which makes the systems weakly parabolic; we will discuss below the inclusion of the newtonian viscosity into the time step.

The maximum time step for hyperbolic systems is limited by the Courant–Friedrichs–Levy (CFL) condition, which is a bound on the maximum distance that information can traverse during a single time step. In our central scheme it is essential that the characteristics emanating from the discontinuities between the piecewise-linear elements remain inside the staggered-grid cell, i.e., that the characteristics do not propagate by a distance longer than half a cell.

In order to convert this requirement into a constraint for the time step, we need to calculate the speeds of the nine characteristics separately for the r - and z -directions. Despite the high dimensionality of the system, the eigenvalues turn out to be easy to calculate; in the r -direction the characteristics speeds, $\lambda_i^{(r)}$, are

$$\lambda_i^{(r)} = -u, -u \pm \sqrt{2(\tau^{rr} + \nu_p/\lambda)}, \quad (42)$$

each triply degenerate. Similarly, in the z -direction

$$\lambda_i^{(z)} = -w, -w \pm \sqrt{2(\tau^{zz} + \nu_p/\lambda)}. \quad (43)$$

Hence, the time step limitation is given by

$$\max_{i,j} [|u_{i,j}| + \sqrt{2(\tau^{rr} + \nu_p/\lambda)}] \Delta t < C \Delta r, \quad (44)$$

$$\max_{i,j} [|w_{i,j}| + \sqrt{2(\tau^{zz} + \nu_p/\lambda)}] \Delta t < C \Delta z, \quad (45)$$

where C is a constant less than one-half.

The parabolic terms in the flow equations are treated with the implicit Crank–Nicholson scheme, which is unconditionally stable. Therefore those terms do not impose an additional time step limitation for the scheme to be stable. One needs, however, to be careful. As pointed out by Minion [32], the combination of parabolic and hyperbolic operators can potentially build up a numerical instability even if each part of the scheme is stable when acting alone. Although this problem can be easily fixed [32] we found no instance in which this fix was necessary.

5. STABILITY

5.1. Linear Stability Analysis: Background

For sufficiently low Taylor numbers (the Taylor number quantities a ratio of inertial to viscous forces), the flow of a newtonian fluid in a Couette cell is described by the azimuthal Couette solution (12). As the Taylor number exceeds a critical value a bifurcation occurs, where the Couette solution becomes unstable, and a new steady-state of superimposed toroidal vortices is reached; these are the well-known Taylor vortices [4]. The threshold of this instability can be found by means of a linear stability analysis: A small perturbation about the primary flow can be decomposed into normal modes, and the amplification rates of these modes are eigenvalues of the linearized equations. This method has become a central paradigm in the analysis of dynamical instabilities.

In the past three decades numerous studies have considered the problem of the viscoelastic Couette–Taylor instability (for reviews see [2, 3]). Most have focused on the modifying effect that elasticity has on the instability threshold. Early work was restricted to the stationary transition. It was found that the critical Taylor number could be raised or lowered, depending on the values of two dimensionless groups: Ψ_1/d^2 and $\Psi_2(R_{in}/d^3)$, where $\Psi_{1,2}$ are the first and second normal stress coefficients and d is the gap width. The critical Taylor number was found to decrease the larger Ψ_1 and Ψ_2 are. The actual value of the second normal stress coefficient in experimentally used fluids is controversial, but it is generally believed to be small and negative; therefore it acts as a stabilizing agent. The most general treatment of the stationary transition [9, 10] was performed for the case of a general “simple fluid” [33].

Walters and co-workers [6–8] studied stability for the Oldroyd-B equation. They found that for strong enough elasticity the unstable stationary mode is overtaken by a new unstable mode, which is oscillatory, or overstable. The Couette solution loses stability at the onset of a Hopf bifurcation, at which the marginally stable amplification rate is imaginary. As the elasticity is further increased the critical Taylor number falls off rapidly.

In recent work Larson, Muller, and Shaqfeh [12, 13, 34] performed experiments followed by stability analyses in the counter limiting regime, in which the inertial forces are negligible and the dynamics are dominated by elasticity; this is the inertia-less, or zero Taylor number limit. They found a critical Deborah number (De) above which Couette flow is unstable.

(The Deborah number is the ratio of a characteristic shear rate and the elastic relaxation rate.) This instability was found to be always oscillatory, with a period of the order of the elastic relaxation time.

Larson *et al.* [34] also considered the effect of the second normal stress difference on these purely elastic modes. For that they modified the Oldroyd-B equation by adding a “second-order term.” Also in this case the effect of small negative values of second normal stress difference is to stabilize the flow. It was further conjectured that this would explain why the purely elastic instability is never observed with high polymer density solutions, in which the second normal stress may be significant.

The major shortcoming of all the aforementioned analyses is their approximate nature; all are based on simplifying assumptions that apply to limiting regimes of parameters. Such approximations are often useful for identifying the essential groupings of parameters that affect the flow properties, thus providing more insight. Only a full stability analysis can, however, resolve the complete structure of the stability spectrum and, in particular, the crossover from the inertial to the elastic regime. Such approximation-free stability analysis was presented by Avgousti and Beris [14] for the Oldroyd-B constitutive equation. They used a pseudospectral method to discretize the radial dependence of the eigenmodes and obtained a generalized complex eigenvalue problem from which all the eigensolutions are readily obtained. Thus they could map the structure of the stability spectrum in the complex- Ω plane, where Ω is the amplification rate of the perturbation.

For zero elasticity all the eigenvalues are real and belong either to a discrete or a continuous spectrum. For finite elasticity they found an additional continuum spectrum lying vertically in the complex plane; its real part is equal to $-1/2 De$. Discrete complex modes seem to detach from this continuum as the elasticity is increased. The exchange of stability, whereby the stationary bifurcation is overtaken by a Hopf bifurcation, occurs as two pairs of complex eigenvalues cross the imaginary axis for a lower Taylor number than is needed to destabilize the least stable real modes. For even larger values of elasticity two other pairs of eigenvalues detach from the continuous spectrum and overtake the previous pairs. This is the exchange of stability between the inertio-elastic modes of Beard *et al.* [8] and the purely elastic modes of Larson *et al.* [12]; thus Avgousti and Beris demonstrated that these two modes belong to different families of eigenfunctions [14].

Avgousti and Beris further analyzed the effect of symmetries on the nature of the bifurcations; group theoretical considerations allow one to characterize the range of possible dynamical behaviors at a bifurcation based only on general symmetry properties and not on the detailed physics of the problem [35, 15]. In particular, there is a theory of Hopf bifurcation with symmetry which gives model-independent information about periodic solutions. In the present problem both the equations of motion and the primary Couette solution are symmetric with respect to azimuthal rotations, axial reflections $z \rightarrow -z$, and both axial and temporal translations. The secondary flow breaks some of these symmetries; the axial and temporal continuous translational invariances are replaced by invariances under only discrete translations; i.e., the new state has lower symmetry.

Because of the symmetries present in the problem the bifurcation is degenerate; for the Hopf bifurcation there are four eigenvalues that become simultaneously unstable at the bifurcation point. This happens because for every solution of the linearized perturbation equation of the form

$$\delta\psi_{\uparrow}(r, z, t) = (\delta u, \delta v, \delta w, \delta\tau^{rr}, \delta\tau^{r\theta}, \delta\tau^{rz}\delta, \tau^{\theta\theta}, \delta\tau^{\theta z}, \delta\tau^{zz})e^{-ikz}e^{\Omega t} \quad (46)$$

there corresponds a second distinct solution,

$$\delta\psi_{\downarrow}(r, z, t) = (\delta u, \delta v, -\delta w, \delta\tau^{rr}, \delta\tau^{r\theta}, -\delta\tau^{rz}, \delta\tau^{\theta\theta}, -\delta\tau^{\theta z}, \delta\tau^{zz})e^{-ikz}e^{\Omega t}, \quad (47)$$

resulting from the z -reflection symmetry of the equations of motion. The complex conjugates of both solutions complete a four-dimensional eigenspace of symmetry-related solutions.

The resulting secondary flow can exhibit two different patterns, each corresponding to a maximal isotropy subgroup [15]. If only one of the two eigensolutions, $\delta\psi_{\uparrow}$ ($\delta\psi_{\downarrow}$) is present, the solution describes a wave of tilted vortices traveling upward (downward). This solution is invariant under the spatio-temporal translation ($t \rightarrow t + \text{Im}(\Omega)\Delta t$, $z \rightarrow z + k\Delta z$). This solution is known as a *traveling*, or *rotating*, *wave*. If, on the other hand, both $\delta\psi_{\uparrow}$ and $\delta\psi_{\downarrow}$ have the same amplitude, the solution describes an axially *standing wave*, which remains invariant under a spatial translation of half a wavelength followed by a temporal translation of half a period, and a reflection about the z -axis. An examination of the standing wave solutions showed that these form a cellular structure that propagates in the radial direction. Vortices are formed in the vicinity of the inner cylinder and move outward until they eventually fade away near the outer cylinder. The intercylindrical gap can be filled with several vortices, the number of those increasing with the gap to radius aspect ratio [13].

Bifurcation theory further establishes that in the event that both traveling and standing wave solutions bifurcate supercritically, one and only one of these two has a stable limit cycle. However, the nature of the bifurcation and the stability properties of the bifurcating branches cannot be predicted solely on the basis of linear stability. For that one needs to resort to a nonlinear analysis.

5.2. Beyond Linear Stability

In order to determine the stability of any bifurcating solution a nonlinear stability analysis is required. Typically, one reduces the partial differential equation into a set of ordinary differential equations through a Liapunov–Schmidt reduction and expands the equations in powers of the bifurcation parameters. The result of such a procedure is a nonlinear equation for the amplitude of the secondary flow. Although this method has been successfully applied to a wide variety of problems, it often involves tedious calculation, in particular when the bifurcation is degenerate.

Rather than performing such a nonlinear analysis, Avgousti and Beris [14] solved the nonlinear system of partial differential equation, treating time as a third dimension, and looking for solutions that have the required symmetries and periodicities. They used, to this end, a spectral method, exploiting the fact that near the bifurcation point accurate results require a relatively small number of modes. Thus they were able to calculate limit cycle solutions both for the traveling and for the standing waves. By examining the dependence of the amplitude of the solution on the bifurcation parameter they established that both branches were indeed supercritical.

With the objective of determining which of the two patterns is the stable one, Avgousti *et al.* [17] developed two algorithms for time-dependent simulations, one for the inertio-elastic regime and one for the purely elastic regime. Both schemes are based on a pseudo-spectral discretization along the radial axis. Rather than initializing the flow with some random noise on top of the primary flow, they used the output of the linear stability calculations to disturb the primary flow by a combination of least stable eigenfunctions, forcing thus either a traveling wave or a standing wave.

Their results are as follows: In the intermediate inertio-elastic regime, initially traveling waves reach a stable limit cycle. Initially standing waves, on the other hand, grow exponentially in amplitude, causing the calculation to break down. Computational limitations did not allow them to determine if any alternative limit cycle is eventually reached. It was only conjectured that a traveling wave would have been recovered. In the purely elastic regime the reverse was found: standing waves are stable, whereas, initially, traveling waves grow in amplitude until a numerical instability is encountered. We remind the reader that all these results were obtained in a computational domain that embodies a single wavelength; the wavelength is hence constrained by the geometry. In addition, mode interactions are suppressed, whereas they may be important in any realistic flow.

In Section 6 we will attempt to resolve some of the questions left open in these earlier studies. In particular we will examine what is the “natural” evolution of the instability when the initial disturbance is random. Also we will check the long-time behavior of an initial perturbation that is symmetric under the isotropy subgroup of the standing wave solution. All our calculations include at least eight natural wavelengths and, therefore, allow for a dynamical selection of the wavelength.

5.3. Linear Stability: A Finite Differences Eigenvalue Solver

Given the set of parameters, η , ω , ν_s , ν_p , and λ , the primary Couette flow is given by Eq. (12). To calculate its stability spectrum we add to it a small disturbance, which is decomposed into its Fourier modes,

$$\begin{aligned}
 u(r, z, t) &= \delta u(r) \sin kz e^{\Omega t} \\
 v(r, z, t) &= v_0(r) + \delta v(r) \sin kz e^{\Omega t} \\
 w(r, z, t) &= \delta w(r) \cos kz e^{\Omega t} \\
 p(r, z, t) &= \delta p(r) \sin kz e^{\Omega t} \\
 \tau^{rr}(r, z, t) &= \delta \tau^{rr}(r) \sin kz e^{\Omega t} \\
 \tau^{r\theta}(r, z, t) &= \tau_0^{r\theta}(r) + \delta \tau^{r\theta}(r) \sin kz e^{\Omega t} \\
 \tau^{rz}(r, z, t) &= \delta \tau^{rz}(r) \cos kz e^{\Omega t} \\
 \tau^{\theta\theta}(r, z, t) &= \tau_0^{\theta\theta}(r) + \delta \tau^{\theta\theta}(r) \sin kz e^{\Omega t} \\
 \tau^{\theta z}(r, z, t) &= \delta \tau^{\theta z}(r) \cos kz e^{\Omega t} \\
 \tau^{zz}(r, z, t) &= \delta \tau^{zz}(r) \sin kz e^{\Omega t},
 \end{aligned} \tag{48}$$

where k is the axial wavenumber and Ω is the amplification rate. Substituting this expansion into the equations of motion and linearizing such to keep only terms that are first-order in the perturbation, we get the set of equations,

$$\begin{aligned}
 \Omega \left(k \delta u - \frac{d}{dr} \delta w \right) &= 2k \frac{v_0}{r} \delta v + \nu_s \left(\frac{d}{dr} \frac{1}{r} \frac{d}{dr} r - k^2 \right) \left(k \delta u - \frac{d}{dr} \delta w \right) \\
 &\quad + k \left(\frac{1}{r} \frac{d}{dr} r \delta \tau^{rr} - k \delta \tau^{rz} - \frac{1}{r} \delta \tau^{\theta\theta} \right) - \frac{d}{dr} \left(\frac{1}{r} \frac{d}{dr} r \delta \tau^{rz} + k \delta \tau^{zz} \right), \\
 \Omega \delta v &= \nu_s \left(\frac{d}{dr} \frac{1}{r} \frac{d}{dr} r - k^2 \right) \delta v - 2 \left(\frac{dv_0}{dr} + \frac{v_0}{r} \right) \delta u \\
 &\quad + \left(\frac{1}{r} \frac{d}{dr} r \delta \tau^{r\theta} - k \delta \tau^{\theta z} + \frac{1}{r} \delta \tau^{r\theta} \right),
 \end{aligned} \tag{49}$$

and

$$\begin{aligned}
\left(\frac{1}{\lambda} + \Omega\right) \delta\tau^{rr} &= 2\frac{v_p}{\lambda} \frac{d}{dr} \delta u \\
\left(\frac{1}{\lambda} + \Omega\right) \delta\tau^{rz} &= \frac{v_p}{\lambda} \left(k \delta u + \frac{d}{dr} \delta w\right) \\
\left(\frac{1}{\lambda} + \Omega\right) \delta\tau^{zz} &= -2\frac{v_p}{\lambda} k \delta w \\
\left(\frac{1}{\lambda} + \Omega\right) \delta\tau^{\theta z} &= \left(\frac{dv_0}{dr} - \frac{v_0}{r}\right) \delta\tau^{rz} + \tau_0^{r\theta} \frac{d}{dr} \delta w + \frac{v_p}{\lambda} k \delta v \\
\left(\frac{1}{\lambda} + \Omega\right) \delta\tau^{r\theta} &= \left(\frac{dv_0}{dr} - \frac{v_0}{r}\right) \delta\tau^{rr} + \left(\frac{\tau_0^{r\theta}}{r} - \frac{d\tau_0^{r\theta}}{dr}\right) \delta u + \tau_0^{r\theta} \frac{d}{dr} \delta u \\
&\quad + \frac{v_p}{\lambda} \left(\frac{d}{dr} - \frac{1}{r}\right) \delta v \\
\left(\frac{1}{\lambda} + \Omega\right) \delta\tau^{\theta\theta} &= 2\left(\frac{dv_0}{dr} - \frac{v_0}{r}\right) \delta\tau^{r\theta} + \left(\frac{2}{r}\tau_0^{\theta\theta} - \frac{d\tau_0^{\theta\theta}}{dr} + \frac{2v_p}{\lambda r}\right) \delta u \\
&\quad + 2\tau_0^{r\theta} \left(\frac{d}{dr} - \frac{1}{r}\right) \delta v.
\end{aligned} \tag{50}$$

The boundary conditions for the perturbation are

$$\delta u = \frac{d}{dr} \delta u = \delta v = 0 \quad \text{for } r = r_L, r_R. \tag{51}$$

Note that the Fourier decomposition (48) includes only modes in which, for example, δu is an antisymmetric function of z . For each solution of the form (48) its symmetric counterpart exists, obtained by the transformation, $\sin kx \rightarrow \cos kx$ and $\cos kx \rightarrow -\sin kx$.

Equations (49) and (50), together with the boundary conditions, form a generalized eigenvalue problem for $\Omega(k)$. One can define a perturbation vector, $\delta \mathbf{x} = (\delta u, \delta v, \delta\tau^{rr}, \delta\tau^{r\theta}, \delta\tau^{rz}, \delta\tau^{\theta\theta}, -\delta\tau^{\theta z}, \delta\tau^{zz})$ and rewrite the equations as

$$\mathbb{A} \delta \mathbf{x} = \Omega \mathbb{B} \delta \mathbf{x}, \tag{52}$$

where \mathbb{A} and \mathbb{B} are operators.

This eigenvalue problem can be solved by discretizing the perturbation vector, $\delta \mathbf{x}$, and expressing the differential operators \mathbb{A} and \mathbb{B} as second-order finite differences; in this representation \mathbb{A} and \mathbb{B} are square matrices. The discrete spectrum, Ω_i , is then solved with a standard eigenvalue solver.

5.4. Results

We first tested the eigenvalue solver and, notably, checked that it is second-order accurate. In Table 1 we list the eigenvalue of the least stable mode for fixed parameters and an increasing number of discretization points, N . The results denoted by $N = \infty$ were obtained by Richardson extrapolation, based on the assumption of second-order convergence; this estimate was then used to evaluate the error as a function of N . The order of convergence

TABLE 1
Evaluation of the Convergence Rate of the Linear Stability Solver

| | $N = \infty$ | $N = 40$ | rate | $N = 48$ | rate | $N = 56$ | rate | $N = 64$ |
|-----|--------------|----------|------|----------|------|----------|------|----------|
| (a) | .00740 | -.00348 | 1.98 | -.00018 | 2.00 | .00183 | 2.03 | .00315 |
| (b) | .00409 | -.00170 | 1.82 | -.00006 | 2.00 | .00104 | 1.89 | .00172 |

Note. The amplification rate of the least stable mode is calculated for increasing number of discretization points. The parameters are $\eta = 0.883$, $\omega = 0$, $v_p/(v_s + v_p) = 0.9$, and (a) $\lambda = 0.3$, $v = (v_p + v_s) = 0.07428$, $k = 1.125$; (b) $\lambda = 1.2$, $v = 0.1299$, $k = 1.430$.

between each pair of data could thus be estimated. The table confirms that the procedure is second-order convergent.

The results of the linear stability calculation are presented in Figs. 4–8. In Fig. 4 we plot the critical Taylor number defined by

$$\text{Ta} = \frac{1}{v^2} \frac{\eta^2}{1 - \eta^2} \quad (53)$$

($v = v_s + v_p$ is the total viscosity) as a function of $\epsilon = \lambda v_p$, a parameter that measures the elasticity. Unlike the Deborah number, ϵ is an intrinsic property of the fluid and depends neither on the cell geometry nor on the flow driving parameters [14]. The fixed parameters

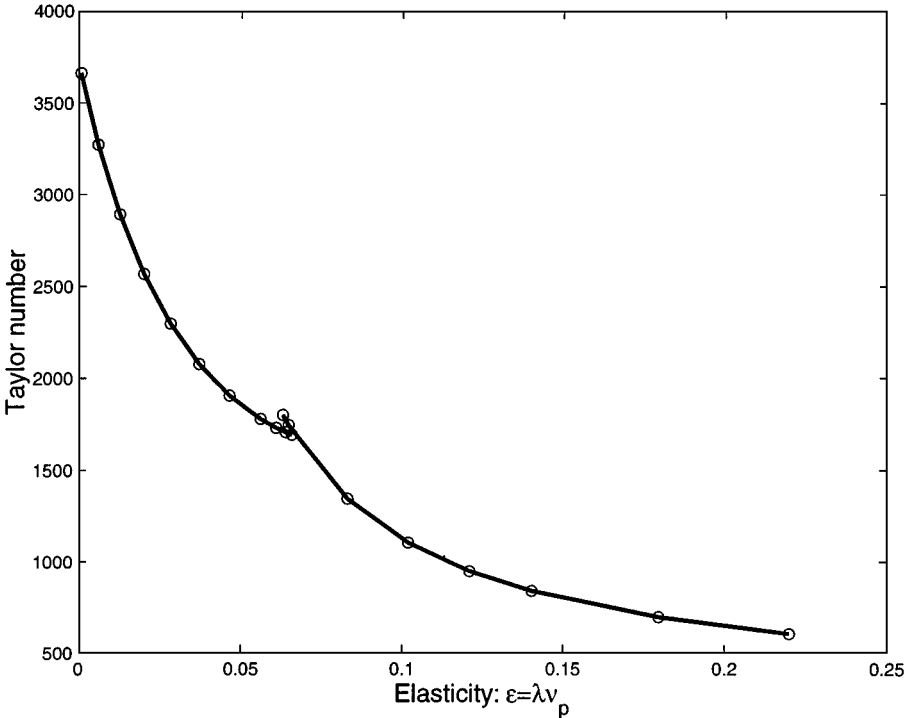


FIG. 4. The critical Taylor number versus the elasticity, $\epsilon = \lambda v_p$, for $\eta = 0.883$, $\omega = 0$, and $v_p/v = 0.9$. The graph shows the neutral curves for two branches of eigenmodes. The weak elasticity mode is stationary, whereas the strong elasticity mode is overstable. A transition between the two modes occurs at a value of elasticity near 0.07.

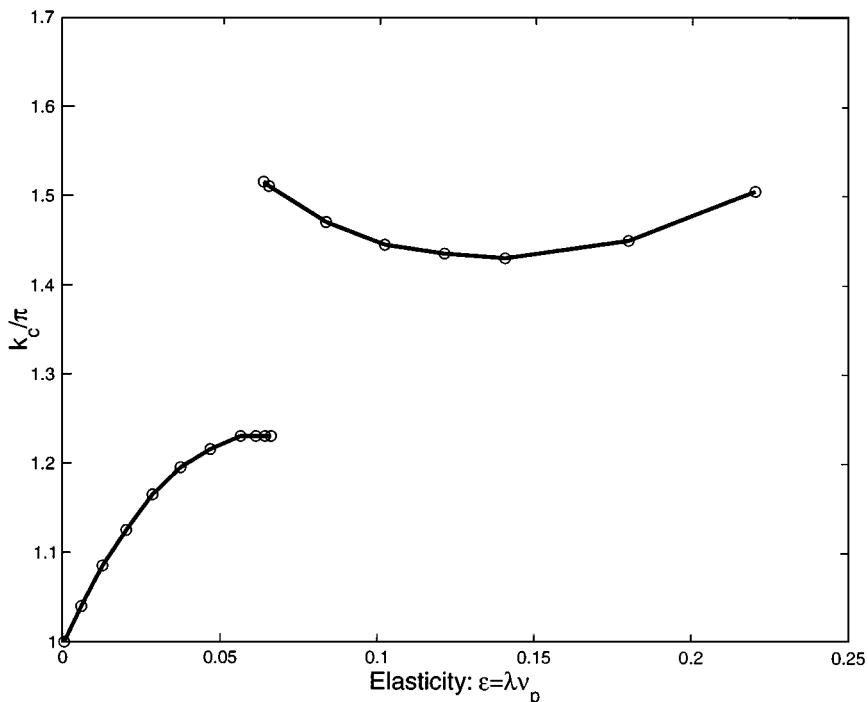


FIG. 5. The critical wavenumber k_c versus the elasticity for the parameters of Fig. 4.

are $\eta = R_{out}/R_{in} = 0.883$, $\omega = \Omega_{out}/\Omega_{in} = 0$, and a viscosity ratio, $v_p/v = 0.9$; the same values of parameters are used in the numerical simulations reported below.

In agreement with Beard *et al.* [8], a stationary bifurcation is found for small values of elasticity, with the critical Taylor number decreasing with increasing elasticity. Above a value of elasticity around 0.07 an overstable mode takes over. The neutral stability curve of the overstable mode decays as a function of the elasticity more rapidly than the stationary transition curve. The intersection of the two neutral stability curves is an exchange of stability point, not a bifurcation point; the two modes are distinct solutions of the perturbation equations.

In Fig. 5 we plot the dependence of the critical wave number k_c on the elasticity. For small values of elasticity the critical wavenumber is close to the newtonian case, $k_c \approx \pi$; i.e., the Taylor vortices have an approximately square cross section. The critical wavenumber increases with the elasticity and reaches a maximum in the vicinity of the exchange of stability point. At this point, where the least stable mode becomes the overstable one, k_c jumps discontinuously from $k_c = 1.230$ to $k_c = 1.525$. The behavior of k_c for the overstable mode is nonmonotonic. These results are in agreement with earlier work (e.g., Fig. 9 in [8]).

Figure 6 shows the oscillation frequency, $\text{Im}(\Omega_c)$, of the marginally overstable mode. At the exchange of stability point the frequency is finite and equals approximately 0.25. The critical frequency increases with the elasticity until it eventually saturates. For even higher values of elasticity it starts to slowly decrease. The critical frequency falls to zero for a value of elasticity slightly below the exchange of stability point; at this point the pair of complex modes bifurcate from a pair of real modes. It is interesting to note that the overstable mode takes over almost as it formed.

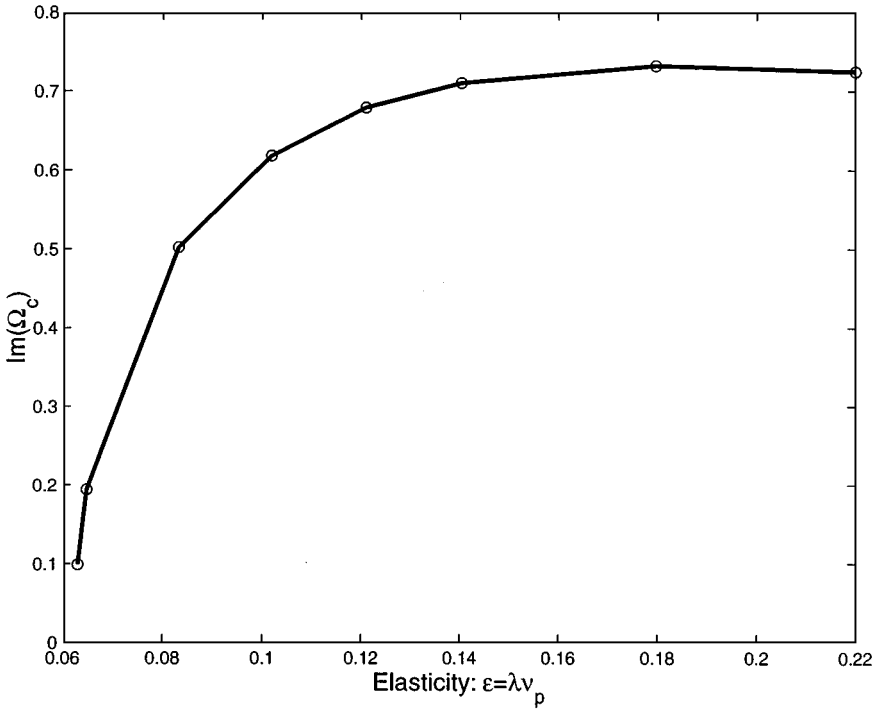


FIG. 6. The critical oscillation frequency of the marginally overstable mode versus the elasticity. The parameters are the same as in Fig. 4.

We next analyze the structure of the eigenvalue distribution in the complex Ω plane. In general, the spectrum is divided into continuous parts and discrete parts. The distinction between the two is manifested as the number of discretization points is raised. Discrete modes keep their identity under refinement, whereas continuum modes do not and their density increases.

Figures 7 and 8 show the stability spectrum of two marginally stable solutions, one at the threshold of a stationary bifurcation (Fig. 7) and one at the threshold of a Hopf bifurcation (Fig. 8). In the first case the least stable eigenvalue is $\Omega = 0$, whereas in the second case a pair of complex eigenvalues crosses the imaginary axis. The calculations were repeated with 48, 56, and 64 discretization points; the resulting eigenvalues are marked by different symbols for each discretization.

Despite the different nature of the bifurcation, the two spectra exhibit very similar properties. There seem to be a small number of discrete modes, which are relatively less stable than continuum modes; hence, these are the modes that affect the stability properties. The continua show interesting geometrical features: one continuum of complex eigenvalues lies on a circle; the center of this circle is an accumulation point of eigenvalues; it is located on the real axis and equals

$$R_0 = -\frac{1}{\lambda(1 - v_p/v)} = -\frac{1}{\lambda_{\text{ret}}}, \quad (54)$$

where λ_{ret} is the so-called retardation time. The radius of the circle is of order $|R_0|$. In [14] the upper-convected Maxwell equation was considered; in that case, where the polymeric viscosity equals the total viscosity, the radius of this circle is infinite. This explains why the structure found in [14] was a straight line rather than a circle.

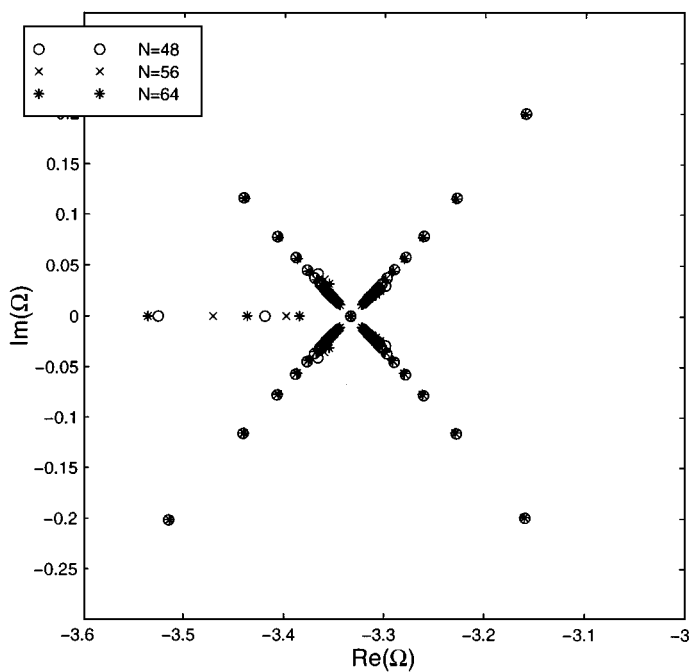
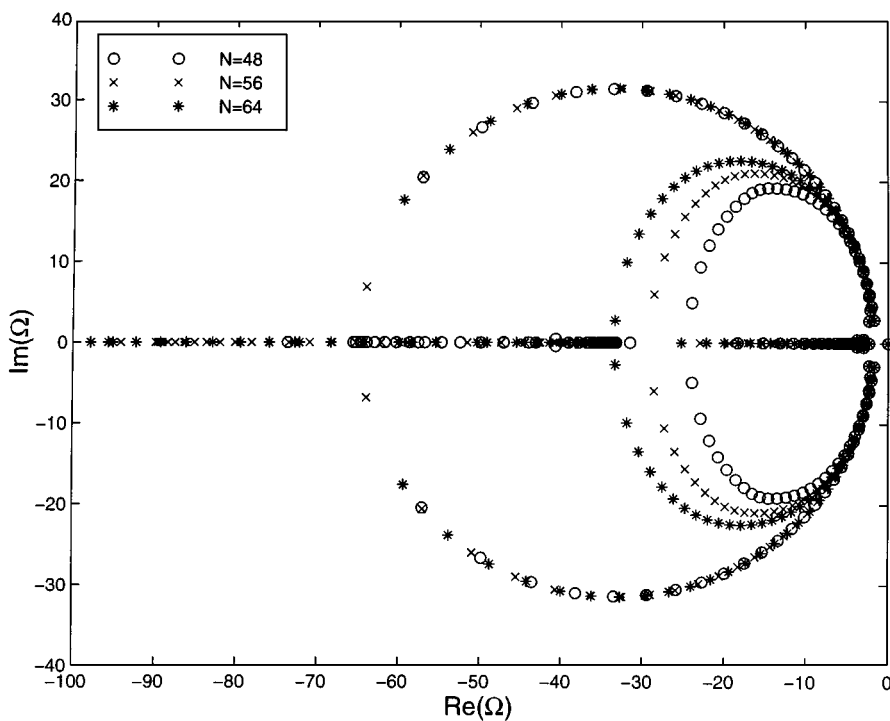


FIG. 7. The distribution of eigenvalues in the complex Ω plane for $\lambda = 0.3$ and $k = 1.125$. The three types of symbols represent calculations performed using 48 (open dots), 56 (crosses), and 64 (stars) discretization points. The parameters correspond to the threshold of a stationary bifurcation, as a real eigenvalue crosses the imaginary axis. Figure (a) shows the principal structure; Fig. (b) shows in more detail the cross-like structure discussed in the text.

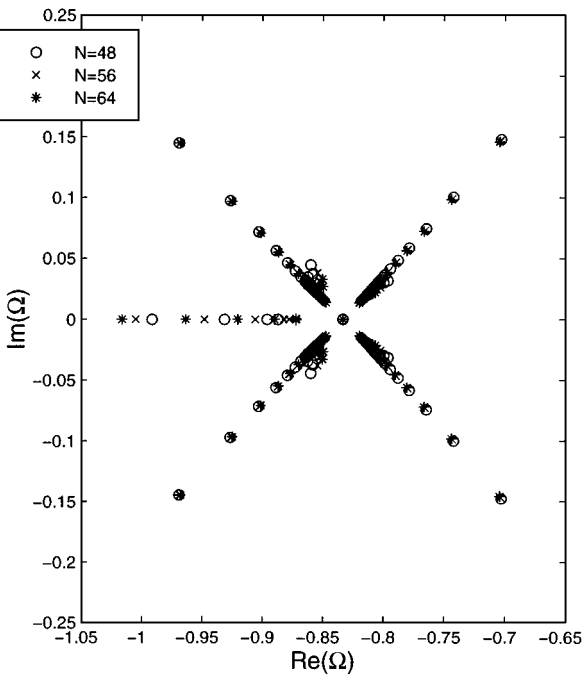
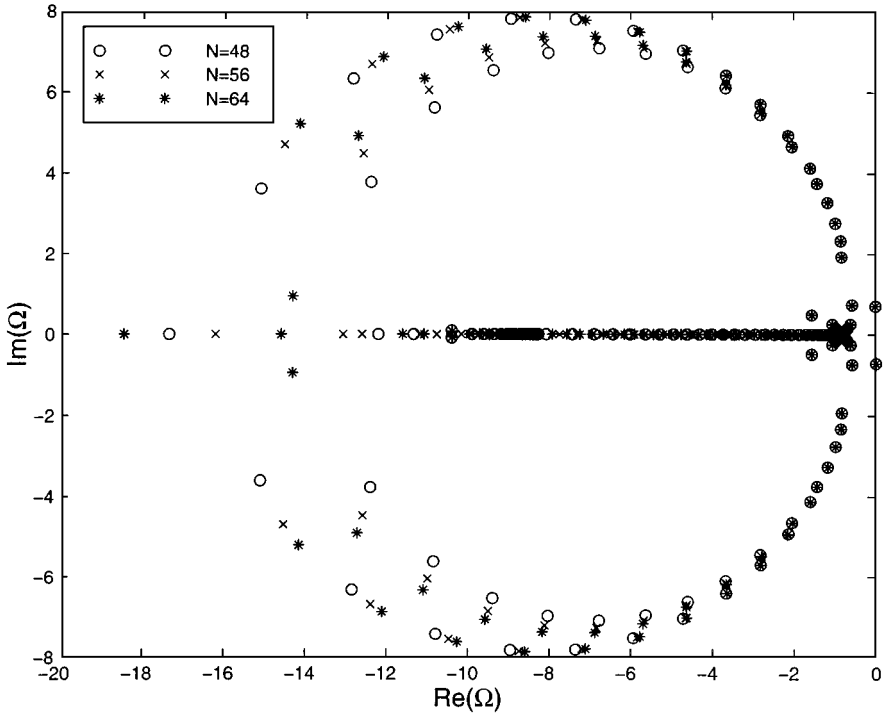


FIG. 8. Same as Fig. 7 for $\lambda = 1.2$ and $k = 1.430$.

Figures 7a and 8a may give the incorrect impression that there are two elliptic structures rather than one circle. An extrapolation of the eigenvalues for increasing refinement shows that the two ellipses converge to the same circle. The reason why not all the eigenvalues can be calculated with the same level of accuracy can be understood as follows. Our method calculates $8N - 6$ modes for an N point discretization. This implies that there will necessarily exist modes in which the number of nodes exceeds N , and therefore badly underresolved. This is the case for the modes forming the spurious additional ellipse. The least stable modes, however, always have a relatively simple structure, and their calculation is therefore accurate.

Another characteristic structure is shown in detail in Figs. 7b and 8b. In both cases there exists a highly degenerate eigenvalue $\Omega = -1/\lambda$; the degeneracy is infinite in the continuum limit. The eigenvalue $\Omega = -1/\lambda$ is the locus of a cross-like structure, which consists of four perpendicular rays that form a 45° angle with respect to the axes. Each ray is terminated at an accumulation point. Thus the stability spectrum is characterized by two special loci; both are real and related to the relaxation and the retardation rates. The former is the center of a cross-like structure, and the latter is the center of a circular continuum.

6. NUMERICAL RESULTS

We now describe the results of the numerical simulations. The scheme was implemented on a Sun Ultra-1 workstation. Most of the calculations were performed for cylinders of $h = 16$ gap units high, discretized on a 32×512 mesh. Each time step takes about 3.5 s; this figure can probably be reduced by a factor of two by optimizing the code. As in the linear stability analysis, all the simulations reported here are for the fixed parameters $\eta = 0.883$, $\omega = 0$, and $v_p/v = 0.9$. For initial conditions we took the primary Couette solution, on top of which we superimposed a small random perturbation.

To test the convergence rate of the scheme we performed the standard analysis, comparing solutions obtained with finer and finer grids. The L_2 norm of the difference of a particular solution with that obtained on a grid twice as fine is our error estimate. By calculating the errors for two levels of refinement and using Richardson extrapolation the convergence rate can be estimated. The result of this analysis for the three flow components is presented in Table 2. These numbers confirm that the scheme is second-order; the measured convergence rate is even higher than two because the asymptotic regime has not yet been reached.

6.1. The Stationary Transition

We first report on simulation results near the onset of the stationary bifurcation for a weakly elastic fluid with $\lambda = 0.3$. Linear stability predicts for these parameters a critical viscosity $v_c = 0.0744$ and a critical wavenumber $k_c = 1.125\pi$.

TABLE 2
 L_2 -Error and Extrapolated Convergence Rates Estimated from the Comparison of 16×64 , 32×128 , and 64×256 Grids

| | $M = 16, N = 64$ | rate | $M = 32, N = 128$ |
|-----------------------------|------------------|------|-------------------|
| $\ u_{M,N} - u_{2M,2N}\ _2$ | 0.0060 | 2.48 | 0.0011 |
| $\ v_{M,N} - v_{2M,2N}\ _2$ | 0.0504 | 2.51 | 0.0069 |
| $\ w_{M,N} - w_{2M,2N}\ _2$ | 0.0074 | 2.42 | 0.0014 |

Note. The parameters are $h = 4$, $v = 0.07$, $\lambda = 0.6$, and the total running time is $t = 20$.

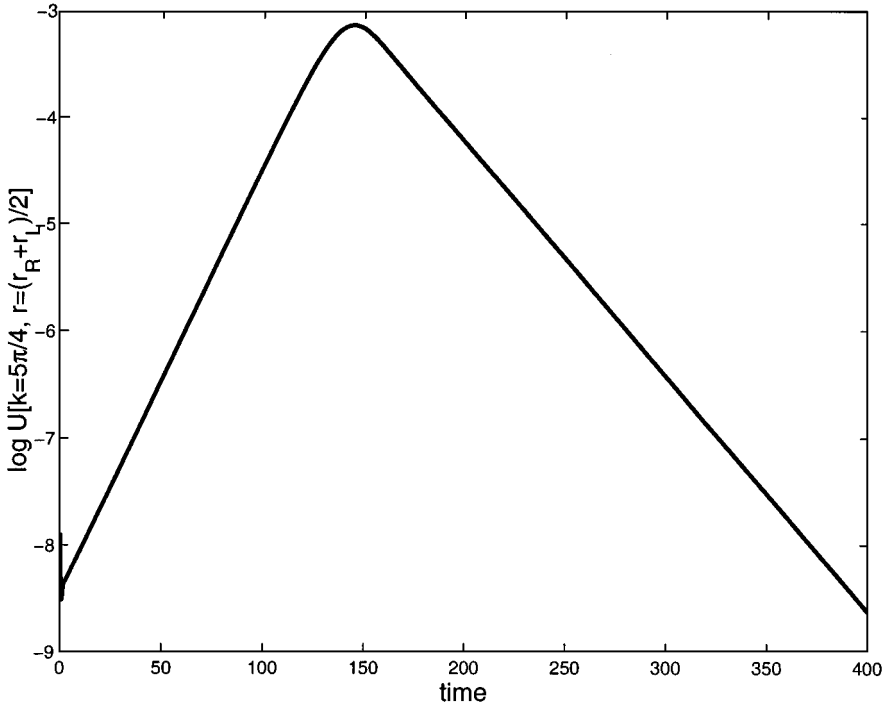


FIG. 9. The logarithm of the amplitude of the Fourier mode $u(k = 5\pi/4)$ versus time, where the radial velocity is measured in the middle of the gap. The parameters are $\nu = 0.073$ and $\lambda = 0.3$. The amplification rate during the early stages of the growth ($t \sim 10$ – 100) is $\Omega = 0.0398$. The linear stability analysis predicts an amplification rate of 0.0359 .

To calculate the amplification rate in the linear regime, we recorded the time evolution of the axial Fourier modes of u in the middle of the gap. In Fig. 9 a semi-logarithmic plot of the amplitude of the $k = 5\pi/4$ mode versus time shows the existence of a long intermediate time interval, $t \sim 10$ – 100 , during which the growth is exponential; the amplification rate of this mode is calculated by a linear fit. As the perturbation evolves, modes start to interact. Eventually a wavelength is selected, and all the modes with wavenumbers that are not multiples of the principal wavenumber decay.

In Table 3 we compare between the amplification rates predicted by the numerical simulations and the linear stability analysis. For both procedures the calculations were repeated for different discretizations, and the results were extrapolated to $M, N \rightarrow \infty$. The table reconfirms the convergence of the results. For $M = 32$ discretization points in the radial axis, the discrepancy in the amplification rate is about 5%; for $M = 64$ it is about 1%.

The flow eventually reaches a new steady state of Taylor vortices very similar to that of newtonian fluids. Because of the periodicity of the domain, the wavelength of the asymptotic pattern must be an integer fraction of the cylinder height. In Figs. 10 and 11 we plot color level images of the velocity and stress components in the steady-state. The number of vortical cells is nine, which corresponds to a wavenumber of $k = 1.125\pi$; this happens to also be the fastest growing mode.

6.2. The Oscillatory Transition

We next study the onset of the oscillatory instability. In Table 4 we list amplification rates of the $k = 3\pi/2$ mode measured in simulations for $\lambda = 1.2$, with $M = 32$ radial discretization

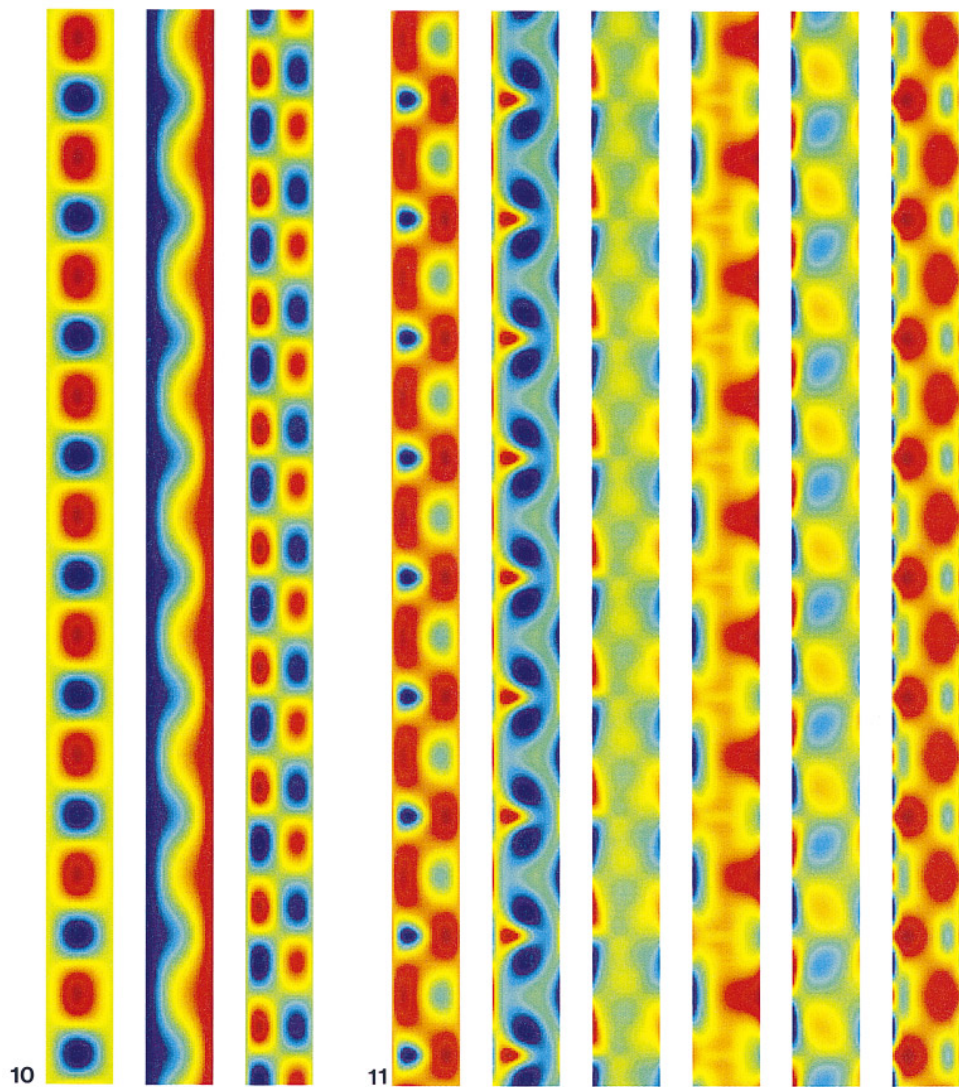


FIG. 10. Color level images of the velocity components, u (left), v (middle), and w (right) for the steady-state Taylor vortices. The blue (red) tones represent high (low) values of the fields. The parameters are $\lambda = 0.3$ and $\nu = 0.073$.

FIG. 11. Color level images of the stress tensor components, τ^{rr} , $\tau^{r\theta}$, τ^{rz} , $\tau^{\theta\theta}$, $\tau^{\theta z}$, and τ^{zz} (from left to right), for the same parameters as Fig. 10.

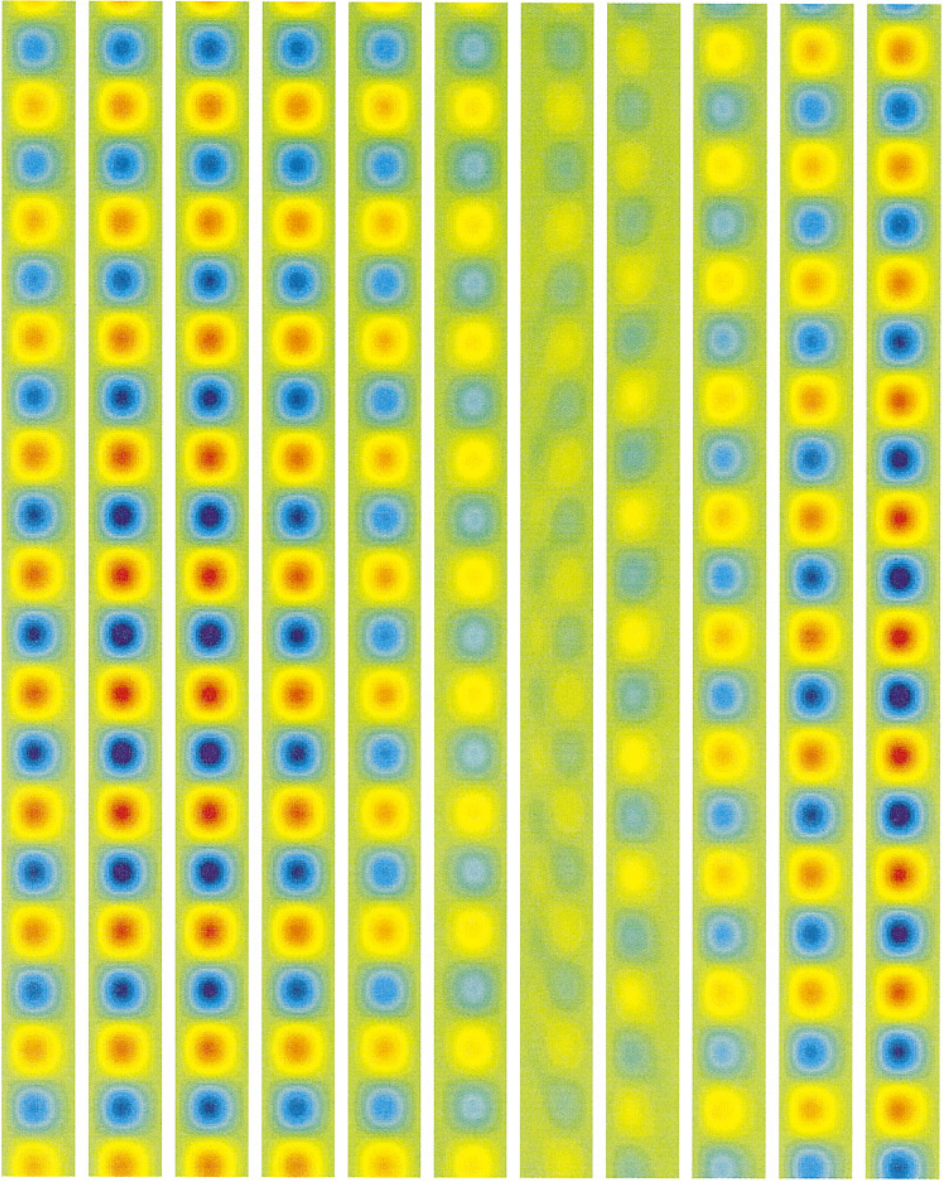


FIG. 13. Time sequence of $u(r, z)$ in the linear regime. The leftmost image is at time $t = 400$; sequential frames are separated by a time interval $\Delta t = 0.5$. This sequence extends over one half of a period. In the middle of this interval, when the amplitude of the secondary flow is small, one can see the vortex moving towards the outer cylinder while a new vortex forms near the inner cylinder.

TABLE 3
The Amplification Rate $\Omega(k = \pi)$ for Different Values of Viscosity

| ν | Simulation | | | | Linear stability | | |
|-------|-----------------|-----------------|-----------------|---------------|------------------|--------|---------------|
| | 16×128 | 32×256 | 64×512 | Extrapolation | 48 | 56 | Extrapolation |
| 0.070 | 0.1309 | 0.1258 | 0.1247 | 0.1243 | 0.1179 | 0.1191 | 0.1224 |
| 0.071 | 0.0986 | 0.0934 | 0.0922 | 0.0918 | 0.0852 | 0.0870 | 0.0920 |
| 0.072 | 0.0657 | 0.0602 | 0.0591 | 0.0587 | 0.0519 | 0.0537 | 0.0586 |
| 0.073 | 0.0320 | 0.0264 | 0.0253 | 0.0249 | 0.0179 | 0.0198 | 0.0250 |

Note. The simulation results are compared to the linear stability results; in both cases the calculation is repeated for discretizations of increasing refinement, and the result is extrapolated to the limit of an infinitely refined mesh. The elastic relaxation time is $\lambda = 0.3$, and the parameters correspond to the vicinity of a stationary bifurcation point.

points. The discrepancy with the extrapolated linear stability results is larger than in the stationary case and attains 20%. This is not surprising as the structure of the eigenmodes is more complicated than in the stationary case and, therefore, requires a finer discretization for a comparable accuracy.

As explained in Section 5, the main issue in the context of the oscillatory instability is the prediction of its evolution, from early stages to, possibly, a stable limit cycle. Earlier work suggests that in the inertio-elastic regime the only stable limit cycle is an axially traveling wave, but so far no conclusive evidence was found. To clarify this point we performed a sequence of long runs for $\lambda = 1.2$. The results are shown in Figs. 12–16.

Useful insight is gained by considering the time evolution of the maximal radial velocity, $u_{\max}(t) \equiv \max_{\mathbf{x}} |u(\mathbf{x}, t)|$ (Fig. 12). The viscosity here is $\nu = 0.126$, whereas the critical viscosity as predicted by linear stability is $\nu_c = 0.1299$. In the early stages ($t \sim 0-700$), u_{\max} oscillates bounded by an exponentially growing envelope. The ratio between the maxima and the minima is large. At about $t \sim 700$ the exponential growth is taken over by an even faster increase which eventually saturates. A new state emerges in which u_{\max} oscillates with a very gradual growth of its envelope. This time the ratio between the maxima and the minima is close to one. This state persists between $t \sim 800-2800$, i.e., during about 200 natural periods. At about $t \sim 2800$ a new transition takes place; this time u_{\max} decreases in amplitude towards a fixed value. This new state remains stable indefinitely. Thus, Fig. 12

TABLE 4
The Amplification Rate $\Omega(k = 3\pi/2)$ for Different Values of the Viscosity

| ν | Simulation | Linear stability | | |
|-------|-----------------|------------------|--------|---------------|
| | 32×256 | 48 | 56 | Extrapolation |
| 0.122 | 0.0607 | 0.0725 | 0.0734 | 0.0759 |
| 0.124 | 0.0474 | 0.0544 | 0.0553 | 0.0578 |
| 0.126 | 0.0336 | 0.0357 | 0.0366 | 0.0391 |

Note. The simulation results are compared to the linear stability results. The elastic relaxation time is $\lambda = 1.2$, and the parameters correspond to the vicinity of the Hopf bifurcation point.

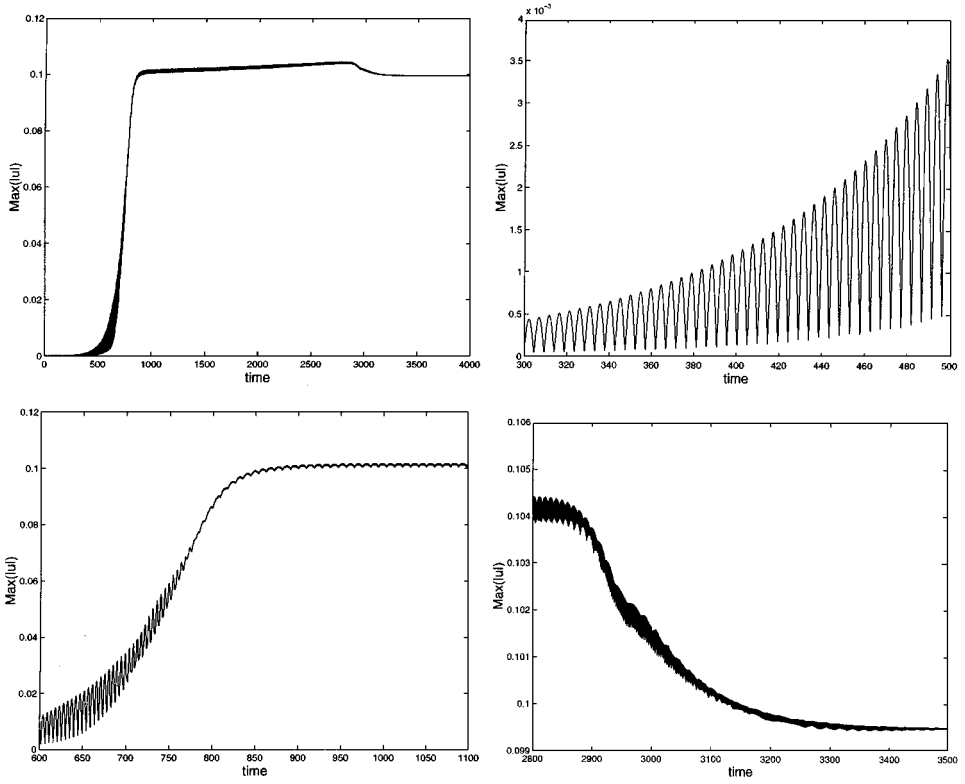


FIG. 12. The maximum value of the radial velocity $\max_x(|u|)$ as function of time. The upper-left graph shows the entire time interval; the three other graphs show in more detail the transitions between the different flow regimes.

indicates the existence of three sequential states: an oscillating exponential growth, a long transitory state, and a stable limit cycle.

To elucidate the nature of these three regimes, we analyzed the evolution of the flow field and the stress tensor as function of time. Below we show sequential snapshots of the radial velocity, $u(\mathbf{x})$, separated by fixed time intervals.

We first consider the early stages of the perturbation. The fact that the secondary flow oscillates with a very high peak-to-peak amplitude ratio is an indication of a standing wave, as confirmed in Fig. 13, in which we show the evolution of $u(\mathbf{x})$ between $t = 400$ and $t = 405$. The vortices have fixed positions (and therefore are referred to as standing waves) and oscillate between positive and negative signs. As described in earlier work, these oscillations are also associated with vortex motion from the inner cylinder outwards.

The early stages of the instability are a linear regime, in which the modes are practically independent. Therefore we expect all unstable modes to grow exponentially; in particular, degenerate modes grow at equal rates. A standing wave is expected in the event that there exists a nearly equal amount of upward- and downward-going waves. In the absence of any preferred direction, this is the likely configuration.

As can be concluded from the time evolution of u_{\max} , the standing wave grows in amplitude until it becomes unstable and is replaced by a new state, which, although not being

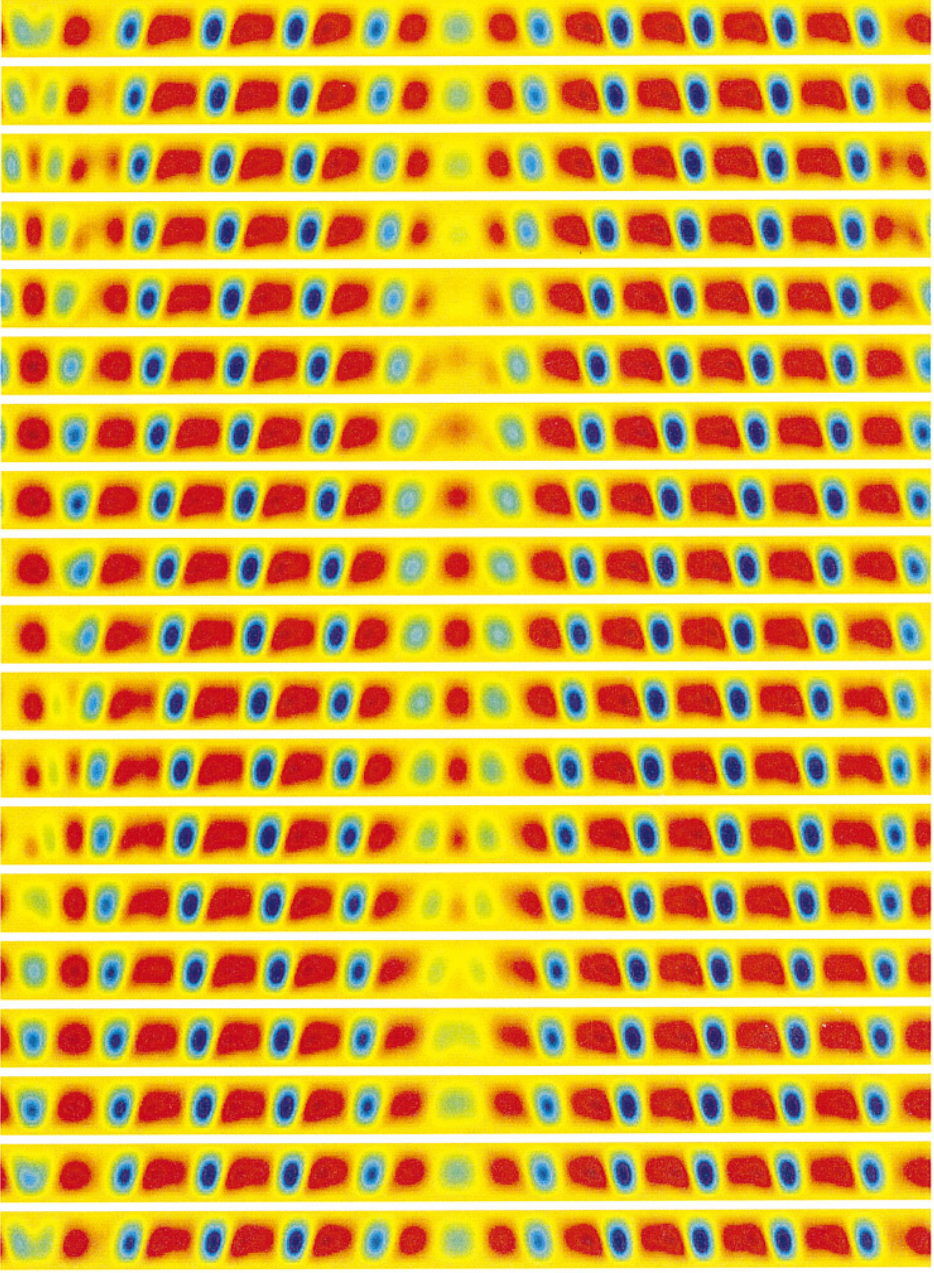


FIG. 14. Time sequence of color level images of $u(r, z)$ in the transient regime. The time sequence runs from left to right, starting at $t = 1300$ with intervals of $\Delta t = 0.5$. In the upper part of the cell three to four vortices are moving upwards, whereas in the lower part of the cell four to five vortices are moving downwards.

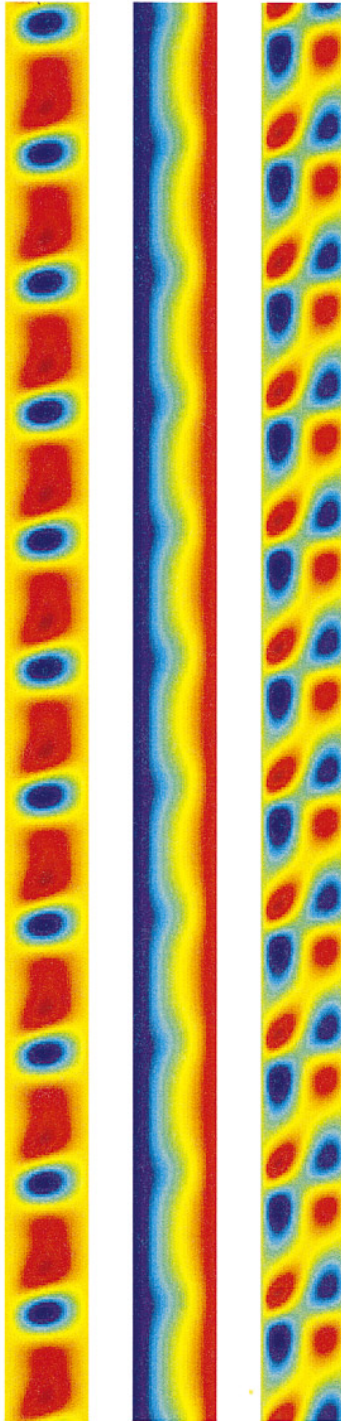


FIG. 15. The three velocity components, u (left), v (center), and w (right) for the stable limit cycle. This structure of inclined vortices moves downward.

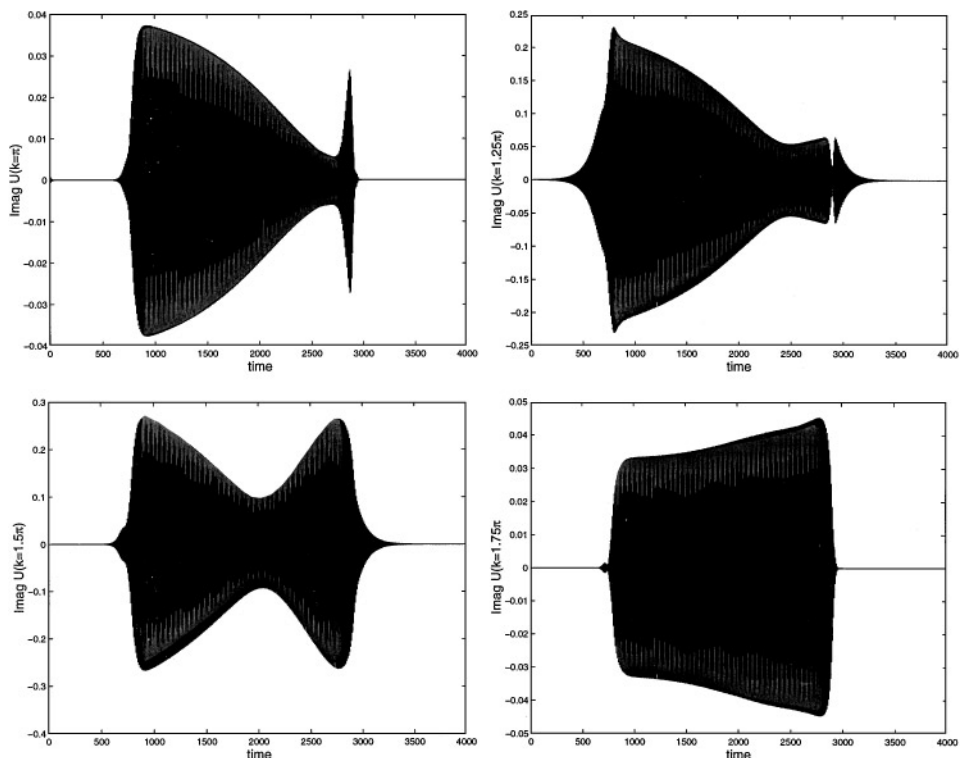


FIG. 16. The imaginary part of the Fourier modes $u(k)$ in the middle of the gap, for (a) $k = \pi$, (b) $k = 1.25\pi$, (c) $k = 1.5\pi$, and (d) $k = 1.75\pi$.

a limit cycle, persists for a long time. The flow pattern associated with this long transient is shown in Fig. 14. The flow decomposes into two distinct regions, exhibiting upward- and downward-going waves, respectively. There exist two special points: one from which the counterpropagating vortices emanate and another into which they merge and annihilate. This transient state persists for hundreds of periods.

These findings confirm the prediction of Avgousti *et al.* [17] that the stable bifurcating branch in the inertio-elastic regime is the traveling wave. What we have found here is that the presence of both upward- and downward-going waves forces a relatively fast breakup of the secondary flow into two subdomains of oppositely traveling waves. The possible occurrence of such a scenario was already anticipated by Larson [3].

The only stable limit cycle is that of a periodic stack of inclined vortices that travel either up or down. This state is eventually reached. The traveling direction in the asymptotic state depends on asymmetries present in the initial conditions. The color level images of the three velocity components is shown in Fig. 15. In this case the vortices are traveling downwards.

Finally, we show in Fig. 16 the time evolution of Fourier modes, $u(k)$, measured in the middle of the gap, for four different wavenumbers k . The four graphs exhibit a similar behavior: The early states are well fitted to exponential growth with a complex amplification rate. The effect of nonlinearities is to suppress the growth. The closer the wavenumber is to the fastest growing mode, the larger is its maximal amplitude. The linear regime is followed by a long transient state during which the modes interact through the nonlinear coupling.

Finally, as the flow reaches a limit cycle a single wavelength is selected and all the other modes decline exponentially.

7. DISCUSSION

We introduced a numerical scheme for viscoelastic flow, which is simple, efficient, and readily adaptable for various (differential) constitutive equations. We implemented it for the viscoelastic Couette–Taylor problem, and we were able to perform calculations that exceed by far previous efforts both in terms of the size of the computational domain and in terms of time intervals. These two factors were crucial for the determination of the natural evolution of the oscillatory instability occurring in the so-called inertio-elastic flow regime.

We found that in the early stages of the instability, linearity results in an exponential growth of all unstable modes; in the absence of axially preferred direction the results is a standing wave, where the vortices are fixed in space and their amplitude oscillates. The prediction of Avgousti *et al.* [17] that the traveling wave solution is the stable one was confirmed. Since our initial conditions include in general comparable amount of upward- and downward-going waves, the secondary flow breaks into two regions, one on top of the other, where in each region a wave of inclined vortices propagates in a different direction. This state can persist for a long transitory time until initial asymmetries cause the selection of either upward- or downward-going wave, and the secondary flow reaches a limit cycle of a fully periodic traveling wave.

While infinite or periodic systems are valuable for the sake of theoretical considerations, real Couette cells are of course finite and closed. It is unclear how the instability evolves in the case of a closed system in which no-slip conditions apply also at the upper and lower boundaries. The fact that counterpropagating waves were found to coexist suggests a possible solution where vortices are created near one of the cylindrical ends, propagate along the axis, and annihilate at the other end. This conjecture will be investigated.

In this paper we have restricted, for convenience, the calculations to an axially periodic computational domain. Thus the implicit parts of the scheme (in connection with the newtonian viscosity and the projection) could be solved using the fast Fourier transform. The extension to a closed domain is in principle not more complicated, except for the need of an efficient method of solving the implicit linear equations; multigrid methods are the natural candidates. To make the scheme adequate for widespread technological use, it is necessary to develop an appropriate methodology for treating more complicated geometries and boundary conditions.

We have focused here on flow within the inertial and the inertio-elastic flow regimes, and disregarded the other limiting case in which the inertial terms are negligible. In order to include purely elastic flow it is necessary to modify the scheme following the example of Beris *et al.* [17]. Such extension is beyond the scope of this paper.

An immediate extension of this present work is to investigate the effect of fluid rheology on the various types of instabilities. In particular, one would like to better understand the effects of shear thinning and second normal stress difference, both absent from the Oldroyd-B equation. Work along these lines is proceeding apace.

ACKNOWLEDGMENTS

I have benefited from many fruitful discussions with Professor M. Denn. I am also thankful to Professors A. Chorin and S. Muller and Drs. A. Kast and D. Nolan for their advice. Dr. D. Adalsteinsson contributed to

the graphical processing of the numerical data. This work was supported by the Applied Mathematical Sciences Subprogram of the Office of Energy Research, Department of Energy, under Contract DE-AC03-76SF-00098.

REFERENCES

1. R. Larson, *Constitutive Equations for Polymer Melts and Solutions*, Chemical Engineering Series (Butterworth, Stoneham, MA, 1988).
2. C. Petrie and M. Denn, Instabilities in polymer processing, *AIChE J.* **22**, 209 (1976).
3. R. Larson, Instabilities in viscoelastic flows, *Rheol. Acta* **31**, 213 (1992).
4. S. Chandrasekhar, *Hydrodynamics and Hydromagnetic Stability* (Dover, New York, 1961).
5. C. Andereck, S. Liu, and H. Swinney, Flow regimes in a circular Couette system with independently rotating cylinders, *J. Fluid Mech.* **164**, 155 (1985).
6. R. Thomas and K. Walters, The stability of elastico-viscous flow between rotating cylinders. Part 1, *J. Fluid Mech.* **18**, 33 (1964).
7. R. Thomas and K. Walters, The stability of elastico-viscous flow between rotating cylinders. Part 2, *J. Fluid Mech.* **19**, 557 (1964).
8. D. Beard, M. Davis, and K. Walters, The stability of elastico-viscous flow between rotating cylinders. Part 3. Overstability in viscous and maxwell fluids, *J. Fluid Mech.* **24**, 321 (1966).
9. C. Miller, *A Study of the Taylor–Couette Stability of Viscoelastic Fluids*, Ph.D. thesis (Univ. Michigan, Ann Arbor, 1967).
10. F. Lockett and R. Rivlin, Stability in Couette flow of a viscoelastic fluid, *J. de Mecan.* **7**, 475 (1968).
11. R. Ginn and M. Denn, Rotational stability in viscoelastic liquids: Theory, *AIChE J.* **15**, 450 (1969).
12. R. Larson, E. S. Shaqfeh, and S. Muller, A purely elastic instability in Taylor–Couette flow, *J. Fluid Mech.* **218**, 573 (1990).
13. E. S. Shaqfeh, S. Muller, and R. Larson, The effects of gap width and dilute solution properties on the viscoelastic Taylor–Couette instability, *J. Fluid Mech.* **235**, 285 (1992).
14. M. Avgousti and A. Beris, Viscoelastic Taylor–Couette flow: Bifurcation analysis in the presence of symmetries, *Proc. Roy. Soc. Lond. A* **443**, 17 (1993).
15. J. Crawford and E. Knobloch, Symmetry and symmetry-breaking bifurcations in fluid dynamics, *Annu. Rev. Fluid Mech.* **23**, 341 (1991).
16. P. Northey, R. Armstrong, and R. Brown, Finite-amplitude time periodic states in viscoelastic Taylor–Couette flow described by the UCM model, *J. Non-newt. Fluid Mech.* **42**, 117 (1992).
17. M. Avgousti, B. Liu, and A. Beris, Spectral methods for the viscoelastic time-dependent flow equations with applications to Taylor–Couette flow, *Int. J. Numer. Meth. Fluids* **17**, 49 (1993).
18. H. Nessayahu and E. Tadmor, Non-oscillatory central differencing for hyperbolic conservation laws, *J. Comp. Phys.* **87**, 408 (1990).
19. X.-D. Liu and E. Tadmor, *Third-Order Nonoscillatory Central Scheme for Hyperbolic Conservation Laws*, Technical Report 96-42, UCLA, 1996.
20. G. Jiang and E. Tadmor, *Non-oscillatory Central Schemes for Multidimensional Hyperbolic Conservation Laws*, Technical Report 96-36, UCLA, 1996.
21. D. Levy and E. Tadmor, *Non-oscillatory Central Schemes for the Incompressible 2-D Euler Equations*, Technical Report 96-37, UCLA, 1996.
22. D. Levy and E. Tadmor, in preparation.
23. R. Kupferman and E. Tadmor, A fast high-resolution second-order central scheme for incompressible flows, *Proc. Nat. Acad. Sci. USA*, in press.
24. A. Chorin, On the convergence of discrete approximations to the Navier–Stokes equations, *Math. Comp.* **22**, 745 (1969).
25. J. Bell, P. Colella, and H. Glaz, A second-order projection method for the incompressible Navier–Stokes equations, *J. Comp. Phys.* **85**, 257 (1989).

26. D. Brown and M. Minion, Performance of under-resolved two-dimensional incompressible flow simulations, *J. Comp. Phys.* **122**, 165 (1995).
27. R. Kupferman, *A Numerical Study of the Axisymmetric Couette–Taylor Problem Using a Fast High-Resolution Second-Order Central Scheme*, Technical Report 40036, LBNL, 1997.
28. B. van Leer, Towards the ultimate conservative difference scheme. V. A second-order sequel to Godunov’s method, *J. Comp. Phys.* **32**, 101 (1979).
29. P. Sweby, High resolution schemes using flux limiters for hyperbolic conservation laws, *SIAM J. Numer. Anal.* **21**, 995 (1984).
30. A. Harten, ENO schemes with subcell resolution, *J. Comp. Phys.* **83**, 148 (1989).
31. X.-D. Liu and S. Osher, Nonoscillatory high order accurate self-similar maximum principle satisfying shock capturing. I, *SIAM J. Numer. Anal.* **33**, 760 (1996).
32. M. Minion, On the stability of Godunov-projection methods for incompressible flow, *J. Comp. Phys.* **123** (1996).
33. B. Coleman and W. Noll, Foundations of linear viscoelasticity, *Rev. Mod. Phys.* **33**, 239 (1961).
34. R. Larson, S. Muller, and E. S. Shaqfeh, The effect of fluid rheology on the elastic Taylor–Couette instability, *J. Non-newt. Fluid Mech.* **51**, 195 (1994).
35. M. Golubitsky, I. Steward, and D. Shaeffer, *Singularities and Groups in Bifurcation Theory* (Springer-Verlag, New York, 1988).